Review

Rare Earth Ion-Doped Vanadate Materials: A Comprehensive Review of Synthesis Strategies, Luminescent Properties, and Sensing Applications

Dragana Marinković *, Giancarlo C. Righini, Maurizio Ferrari *

Posted Date: 13 March 2026

doi: 10.20944/preprints202603.1041.v1

Keywords: rare earth; vanadate; synthesis; luminescence; downconversion; upconversion; sensing applications

 doi:10.20944/preprints202603.1041.v1

Review

Rare Earth Ion-Doped Vanadate Materials: A Comprehensive Review of Synthesis Strategies, Luminescent Properties, and Sensing Applications

Dragana Marinković [1,*], Giancarlo C. Righini [2], Maurizio Ferrari [3,*]

[1] Vinča Institute of Nuclear Sciences, National Institute of the Republic of Serbia, University of Belgrade, P.O. Box 522, 11001 Belgrade, Serbia

[2] Nello Carrara Institute of Applied Physics (IFAC CNR), Sesto Fiorentino, 50019 Firenze, Italy

[3] Institute of Photonics and Nanotechnologies (IFN CNR, CSMFO Laboratory) and FBK Photonics Unit, Via alla Cascata 56/C, Povo, 38123 Trento, Italy

* Correspondence: draganaj@vin.bg.ac.rs (D.M.); mferrari@fbk.eu (M.F.)

Abstract

In recent years, rare earth (RE) ion-doped vanadate materials have garnered significant attention due to their promising applications in everyday technologies. Vanadate-based compounds, typically containing V^{5+} ions within oxide structures, form VO_4 tetrahedra that enable broad ultraviolet absorption and wide-range visible light emission. These materials serve as versatile hosts for RE ions, namely, the 15 lanthanides (lanthanum (La) to lutetium (Lu)) plus scandium (Sc), and yttrium (Y), which act as luminescent centers when incorporated into the matrix. The unique electronic configuration of RE ions, particularly their unpaired 4f electrons, makes them ideal for diverse applications in luminescence, magnetism, electronic and magnetic relaxation, and catalysis. While RE ions exhibit sharp and intense emission peaks in the visible and near-infrared regions, vanadate hosts contribute broad-band spectra through charge transfer transitions within the VO_4 units. These complementary luminescent properties are critical for the advancement of optoelectronic devices. To enhance performance and broaden the applicability of RE-doped vanadate materials, ongoing research focuses on developing innovative synthesis techniques and structural designs. This paper presents a comprehensive review of recent progress in synthesis strategies, luminescent behavior, and sensing applications of RE ion-doped vanadate materials.

Keywords: rare earth; vanadate; synthesis; luminescence; downconversion; upconversion; sensing applications

1. Introduction

Vanadates represent a family of inorganic compounds containing vanadium ion in its highest oxidation state (+5). The most basic member of this group is the tetrahedral orthovanadate ion, VO_4^{3-}, commonly encountered in sodium orthovanadate or in alkaline solutions of V_2O_5 at pH values above 13 [1]. There are various group of vanadate-based materials: orthovanadates (M_3VO_4), pyrovanadate ($M_4V_2O_7$) and metavanadates (MVO_3), often involving metals M = Na, K, Ca, or Bi or rare earth (RE) elements. Among them, RE (Eu^{3+}, Sm^{3+}, Dy^{3+}, Ho^{3+}, Nd^{3+}, Er^{3+}, Yb^{3+}, etc.) doped orthovanadate such as yttrium orthovanadate (YVO_4), gadolinium orthovanadate ($GdVO_4$) and lutetium orthovanadate ($LuVO_4$), have attracted considerable attention due to their strong luminescence, long fluorescence lifetime, low threshold, large emission cross section and high absorption coefficient [2,3].

Rare-earth orthovanadates, expressed by the formula $REVO_4$ (where RE represents La–Lu, Y, or Sc), serve as versatile hosts for incorporating optically active trivalent ions. Because these dopant ions share the same +3 oxidation state and exhibit close similarities in ionic size, electronegativity, and electronic configuration with the rare-earth cations of the lattice, they can be introduced across a

 doi:10.20944/preprints202603.1041.v1

broad concentration range. This substitution occurs without causing significant distortions or alterations in the crystal structure [4].

In addition, incorporation of multiple optically active dopants into orthovanadate matrix is essential for enhancing both the performance and versatility of the matrix. By incorporating various co-dopants, researchers are exploring their potential as sensitizers and their ability to expand the functional properties of the medium. These investigations aim to achieve advanced effects such as self-Q-switching, self-mode-locking, self-frequency-doubling, and self-Raman conversion, thereby broadening the operational capabilities of the system [5]. $REVO_4$ doped with optically active trivalent ions is known for its strong luminescent behavior, which arises from efficient energy transfer processes between the vanadate groups and the dopant ions. By carefully choosing the type and concentration of these dopants, a broad spectrum of emission colors can be achieved. Both undoped and doped $REVO_4$ systems have been widely investigated as multifunctional materials. Their versatility makes them highly appealing for diverse applications, including use in phosphors, specialty glasses, optical polarizers, and optoelectronic devices. They also play important roles in telecommunications, scintillation detectors, and photocatalysis. Furthermore, $REVO_4$ compounds show promise as advanced sensing nanoprobes, offering dual functionality for optical bioimaging and magnetic resonance imaging (MRI) [6,7].

The YVO_4 material stands out among orthovanadates as one of the most extensively studied laser materials over the past few decades. Its unique physical characteristics makes it highly valuable in diverse applications, ranging from polarizers and gas sensors to phosphors and advanced laser systems, particularly when doped with trivalent rare-earth ions [8]. Also, YVO_4 exhibits remarkable chemical stability along with a broad optical transparency range from 400 to 5000 nm. Owing to these properties, it has found extensive use in optical communication systems and is a key material in the development of light isolators and circulators [9]. Rare-earth–doped $LuVO_4$ materials demonstrate exceptional laser performance, attributed to their stronger absorption at pump wavelengths and enhanced emission cross-sections compared to other orthovanadates. In particular, neodymium-doped $LuVO_4$ (Nd:$LuVO_4$), which crystallizes in the zircon structure, offers a significantly larger emission cross-section than Nd:YVO_4 and Nd:$GdVO_4$, while also maintaining a high threshold for optical damage [10] .

On another side, $GdVO_4$, with its exceptionally high melting point at ~ 1800 °C, offers several advantages over YVO_4. It delivers greater brightness, responds efficiently to ultraviolet excitation, and facilitates effective charge-transfer processes. In addition, $GdVO_4$ exhibits lower phonon energy, reduced sensitivity to moisture, and can serve in multiple applications either in its undoped form or when doped with optically active trivalent lanthanide ions [11,12].

Materials based on Gd^{3+} ($4f^7$) ions serve as excellent lattice hosts for developing up-conversion systems, largely because their lowest excited states lie at relatively high energies. The luminescent behavior of $GdVO_4$ strongly depends on the rare-earth ions incorporated into its lattice. Doping with Eu^{3+}, Dy^{3+}, or Sm^{3+} enables the material to act as an efficient down-converter. In contrast, introducing ions such as Er^{3+}/Yb^{3+}, Ho^{3+}/Yb^{3+}, Tm^{3+}/Yb^{3+} or complex mixtures like $Er^{3+}/Tm^{3+}/Ho^{3+}/Yb^{3+}$ generates a broad range of up-conversion emission colours [13]. Furthermore, Nd^{3+} doping expands its luminescent potential, adding another dimension to its versatility. Neodymium-doped $REVO_4$ compounds combine strong mechanical stability with excellent optical performance, particularly through their pronounced absorption at 808 nm. This wavelength is highly relevant for biomedical technologies, making such materials especially attractive in that field. In addition, nanoscale phosphors derived from $GdVO_4$ and co-doped with rare-earth ions such as Nd^{3+} and Yb^{3+} can act as colloidal donor–acceptor systems. These nanophosphors provide a useful platform for investigating interparticle energy transfer phenomena in aqueous nanofluids [14]. Also, Gd-based materials can be used in osteogenic, antimicrobial, anticancer applications, and in bioimaging and bioprobes. This functionality arises from the presence of unpaired electrons in Gd^{3+} ions, which effectively alter the relaxation dynamics of nearby water protons, thereby enhancing image contrast [15].

 doi:10.20944/preprints202603.1041.v1

This paper presents a comprehensive review of recent progress in synthesis strategies, luminescent behavior, and sensing applications of RE ion-doped vanadate materials.

2. Materials and Methods

The fabrication of vanadate based materials with high purity, crystallinity, and well-defined uniform size, morphology, and composition along with a homogeneous distribution of impurities is crucial for the advancement of modern functional materials. To be practical, synthetic methods must also be economical, scalable to industrial production, and capable of delivering high yields. These requirements drive the development of novel or modified synthesis procedures aimed at enhancing the characteristics and performance of different kinds of vanadate materials.

In recent years, the design, synthesis, and fabrication of multifunctional materials have gained significant attention. A variety of synthetic approaches can be employed to produce $REVO_4$ with diverse sizes, shapes, properties, and morphologies, depending on the intended application. Control over nanoparticle size and shape is typically achieved through careful optimization of reaction parameters. Furthermore, synthesis methods can be classified based on the phase in which the phosphors are formed, i.e., solid, liquid, or gaseous, providing different pathways to tailor their structural and functional properties.

2.1. Solid State Reaction

Inorganic solids are often synthesized by the ceramic method, which involves mixing stoichiometric amounts of solid precursors, grinding them to fine particles, and heating for several hours. For example, the simplest reaction pathway yields $GdVO_4$ by combining gadolinium oxide (Gd_2O_3) with vanadium pentoxide (V_2O_5):

$$Gd_2O_3+V_2O_5 \rightarrow 2GdVO_4$$

This process requires high temperatures to enable ion diffusion, but the large difference in melting points between V_2O_5 (681 °C) and Gd_2O_3 (2339 °C) complicates synthesis. While diffusion can be aided by fine grain size and mixing, elevated temperatures remain essential. A challenge arises from V_2O_5 volatility and decomposition at high temperatures, which can lead to oxygen loss and formation of VO_2. Literature reports vary: some note incomplete reactions with stoichiometric mixtures, while others suggest adding excess V_2O_5 or carefully controlling heating ramps to avoid evaporation. For example, slow heating to 950 °C followed by higher temperatures can stabilize the reaction. To address these limitations, precursors must be thoroughly mixed to maximize surface contact. In some cases, reactions are carried out under vacuum or in an inert atmosphere, which can further accelerate the process. Ultimately, thorough characterization of the product is necessary, as impurities such as unreacted Gd_2O_3, $GdVO_3$, or non-stoichiometric $GdVO_4$ may form due to volatility and reduction of V_2O_5 [16,17].

For example, $REVO_4$ (RE =Y, Sm, Gd, Yb, Lu) and $GdVO_4$:Ho^{3+}/Yb^{3+}materials are typically synthesized in the solid phase using a high-temperature solid-state method. In this process, stoichiometric amounts of precursors are thoroughly ground, mixed, and heated in multiple steps at approximately 1200 °C for several hours to ensure complete reaction and formation of the desired product [18,19].

2.2. Coprecipitation Method

The coprecipitation method is a simple and effective technique for synthesizing vanadate-based materials with uniform size distribution. The process involves dissolving precursor salts (nitrates, sulfates, chlorides, etc.) in water, adding a precipitating agent (hydroxide, carbonate, or hydrogen carbonate), followed by aging, separating the precipitate, and finally washing and drying. The precipitation rate depends on the specific metal ions used. Huignard et al. demonstrated that Eu-doped YVO_4 materials can be synthesized at room temperature by coprecipitation from soluble nitrates and sodium orthovanadate. Although their work focused on nanoparticles, the findings—

 doi:10.20944/preprints202603.1041.v1

aside from size control—apply to bulk materials. The reaction is highly pH-dependent, with yttrium orthovanadate forming only within a narrow range (12.5–13.0). At pH values above 13, hydroxides precipitate without reacting, while acidic conditions favour condensed vanadates, preventing orthovanadate formation [20].

The reaction involves in a first step the precipitation of the kinetically favored hydroxide:

$$(Y_xEu_{1-x})^{3+} + 3OH^- \longrightarrow Y_xEu_{1-x}(OH)_3 \downarrow$$

which, in a second step, reacts with orthovanadate to form thermodynamically stable $Y_xEu_{1-x}VO_4$:

$$Y_xEu_{1-x}(OH)_3 + VO_4^{3-} \longrightarrow Y_xEu_{1-x}VO_4 + 3OH^-$$

Subsequent studies suggest that similar conditions apply to Gd^{3+} systems, as rare earth hydroxides are generally insoluble in water but soluble in acids. For bulk reference materials, precise particle size control is unnecessary, and solution synthesis offers the advantage of ambient temperature processing, avoiding issues linked to high-temperature solid-state methods. However, rapid precipitation often produces defective crystalline regions. Thermal treatment has been shown to improve crystallinity, making a two-step process, coprecipitation followed by heating at different temperatures, a viable alternative to ceramic synthesis, while avoiding complications from V_2O_5 volatility [13].

2.3. Hydrothermal/Solvothermal Method

Hydrothermal (or solvothermal) synthesis relies on dissolving inorganic substances in water or another solvent at temperatures above 100 °C and pressures around 1 atm, followed by crystallization. The key difference is that hydrothermal methods use water, while solvothermal methods employ other solvents. $REVO_4$ can be readily prepared this way, though high-temperature calcination is required to enhance luminescence. Reaction parameters such as pressure, temperature, pH, and precursor ratios determine the morphology and size of the final product [21]. The hydrothermal synthesis method provides significant advantages for producing vanadates through multiphase or liquid-phase chemical processes. However, it has notable drawbacks: need of costly autoclaves, safety risks during reactions, and difficulty of monitoring processes directly [21].

For example, $GdVO_4:Yb^{3+}/Er^{3+}$ nanoparticles produced hydrothermally are often coated with SiO_2 before calcination to prevent growth and aggregation; the coating can later be removed by NaOH etching. Using trisodium citrate (Na_3Cit) as a chelating agent, $GdVO_4$ nano- and microcrystals with varied morphologies, crystal orientation and defects, have been synthesized [22,23].

2.4. Sol-Gel Route

Sol-gel synthesis is a versatile wet-chemical method that can be performed through routes such as alkoxide hydrolysis, inorganic gelation, or polymerizable complex processes. It enables molecular-level mixing of precursors, offering advantages over solid-state reactions, including uniform dopant distribution, lower synthesis temperatures, reduced contamination, and control over porosity. Drawbacks include difficulty in removing organic groups and risk of cracks in the final material. Chelating agents play a crucial role, as their type and combustion properties influence the physico-chemical characteristics of the products [24]. The sol-gel method is highly valued due to its relatively low initial cost for producing high-quality materials, its ability to design and control the chemical structure of substances, and its capacity to achieve uniform composition with a large surface area. Despite these advantages, the technique has limitations, including extended reaction times and considerable shrinkage during the dehydration stage [25].

In practice, $GdVO_4$ is often synthesized from $Gd(OAc)_3$ and NH_4VO_3 dissolved in water, mixed in the proper molar ratio with carboxylic acids (e.g., citric, malic, or tartaric acid), then heated with stirring to form a gel. The gel is dried to yield a carboxylate precursor, which is subsequently calcined. In some cases, synthesis can proceed without carboxylic acids. Using different acids allows production of vanadate with different size and morphologies. For example, tartaric acid can serve both as a chelating agent and combustion fuel, with calcination temperature and precursor ratios directly affecting particle size and crystallinity [26].

 doi:10.20944/preprints202603.1041.v1

2.5. Microwave-Assisted Method

Microwave synthesis employs electromagnetic radiation (0.3–300 GHz) to rapidly decompose precursors and trigger fast nucleation, producing small nanoparticles in a much shorter time. A key requirement is that at least one precursor must absorb microwaves. This method is often combined with hydrothermal synthesis. Microwave irradiation plays a vital role in accelerating reaction kinetics by enabling rapid initial heating, which significantly increases overall reaction rates. This technique produces cleaner products, ensures faster consumption of starting materials, and improves yields. Another advantage lies in the uniform heating and precise control of process parameters, which enhance reproducibility and reliability of reaction conditions. In the field of vanadate synthesis, microwave heating represents a novel and uniform approach that deserves further development. Using of green reaction media not only shortens reaction times but also minimizes chemical waste, making it an attractive and sustainable method [27]. Typically, $Gd(NO_3)_3{\cdot}6H_2O$ and NH_4VO_3 solutions are mixed with EDTA at high pH, stirred, and placed in a microwave reactor at 150 °C for 180 minutes. The resulting powders are collected by centrifugation, washed with water and ethanol, and dried [28,29].

3. Results

3.1. Crystal Structure of the AVO_4 Materials

Materials of the type AVO_4 (where A = Sc, Y, Bi, or any of the lanthanides La–Lu) adopt a tetragonal zircon-type crystal structure, similar to $ZrSiO_4$. In this arrangement, the V^{5+} ions within the VO_4^{3-} groups are tetrahedrally coordinated by O^{2-} ions, while the trivalent A^{3+} cations are surrounded by eight O^{2-} ions. The three-dimensional framework is built from alternating AO_8 distorted dodecahedra in which the A^{3+} cations occupy a non-centrosymmetric crystallographic site with D_{2d} symmetry that share edges with tetrahedral VO_4. As example, the tetragonal crystal structure of $GdVO_4$ is presented in Figure 1. This connectivity results in chains of vanadium ions aligned parallel to the c-axis. Bond distances vary within the structure: there are four shorter (2.33 Å) and four longer (2.45 Å) A–O bonds, whereas V–O bonds are all 1.74 Å long, consistent with tetrahedral coordination of V^{5+} ions. Each O^{2-} ion is bonded to two equivalent A^{3+} cations and one V^{5+} ion. Importantly, substitution of different A^{3+} ions does not alter the crystal type, as all AVO_4 compounds are isostructural. For example, YVO_4 compound parameters are: a = 7.13 Å, b = 7.13 Å, c = 6.30 Å, $\alpha = \beta = \gamma = 90°$ and unit cell volume V = 320.53 Å^3 [30]. Many rare-earth vanadates exhibit a low-temperature Jahn–Teller distortion, in which their tetragonal crystal structure transforms into an orthorhombic geometry. Interestingly, this type of crystallographic transition has not been observed in YVO_4 or in $GdVO_4$ [31].

Also, the lattice distortion can be induced by the incorporation of dopant (for example Eu^{3+} ions) into the host crystal structure. The unit cell volume exhibits a slight increase as the concentration of dopant ions rises. Figure 2 depicts difference in the structural configuration of the monoclinic $LaVO_4$ and $Y_{0.5}La_{0.5}VO_4$ structures doped with Bi^{3+} together with Rietveld refinement. In the $LaVO_4$ structure, La atoms are coordinated in a hexahedral arrangement with six oxygen atoms, while V atoms are coordinated to four oxygen atoms, forming a tetrahedral geometry. This host lattice contains two types of cations: La^{3+} with ionic radius r = 1.16 Å and V^{5+} with ionic radius r = 0.35 Å, for coordination number 8. The dopant ion Bi^{3+} (with ionic radius r = 1.17 Å) for the coordination number 8, shares the same valence state as La^{3+} and exhibits similar ionic sizes and coordination environments and preferentially substitutes at La^{3+} sites within the lattice. The $Y_{0.5}La_{0.5}VO_4$ structure crystalizes in tetragonal zircon-type crystal structure, as it was mentioned and explained above for $GdVO_4$ [32–34].

 doi:10.20944/preprints202603.1041.v1

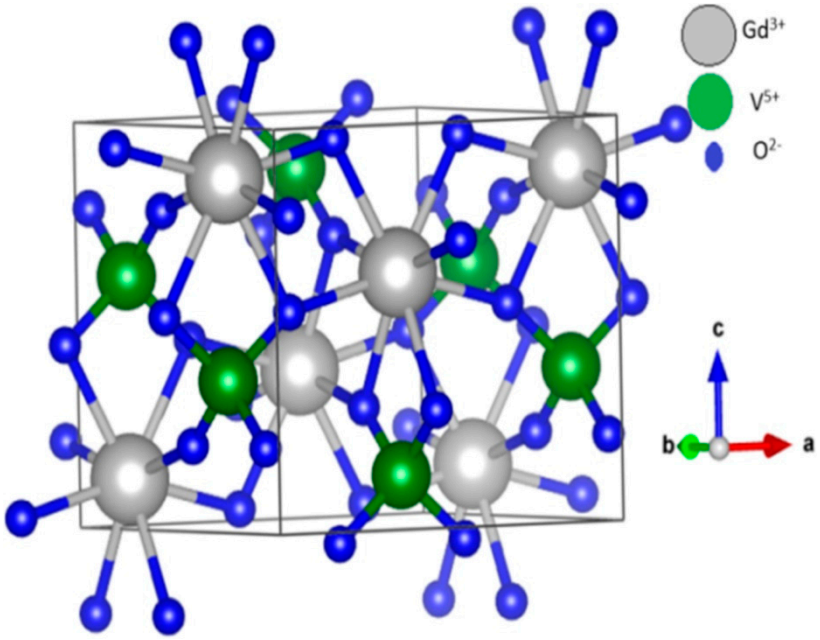

Figure 1. Tetragonal crystal structure of $GdVO_4$. Reproduced from Ref. [30] under Institute of Physics and IOP Publishing license.

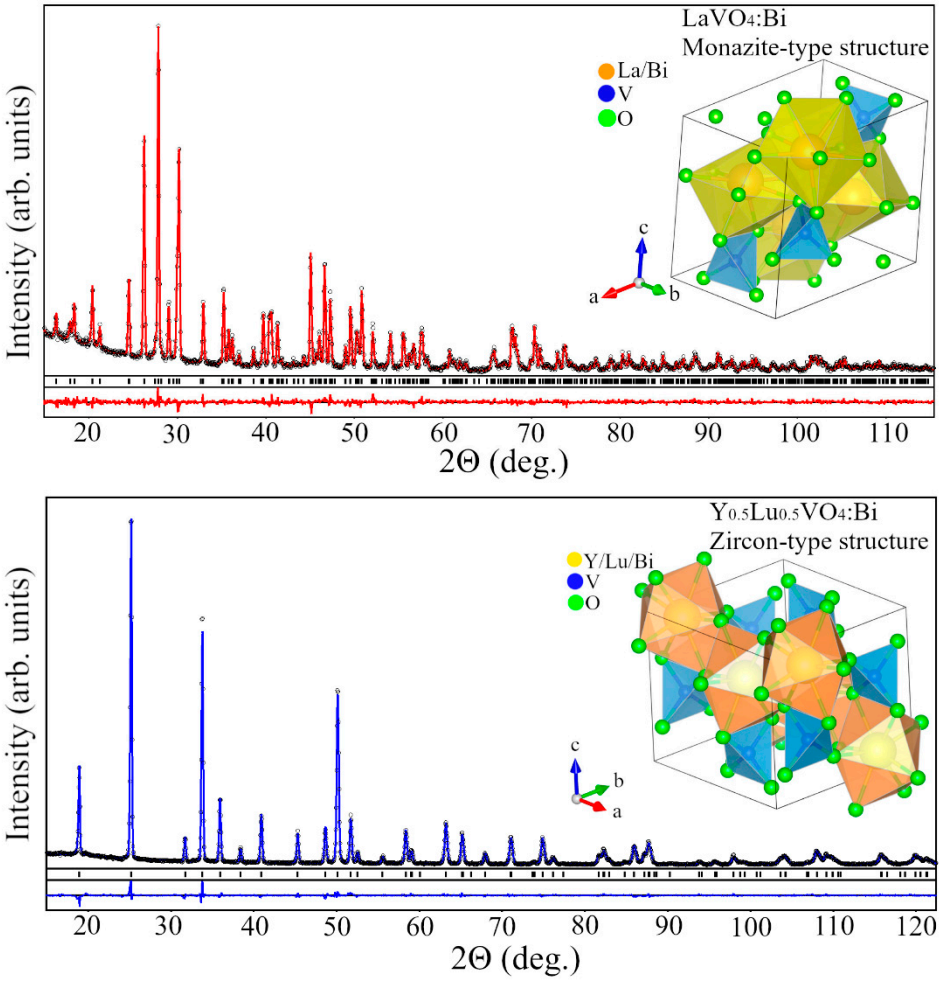

Figure 2. Graphical results of Rietveld refinement of Bi-doped $LaVO_4$ (top) and $Y_{0.5}Lu_{0.5}VO_4$ (bottom) structures. Experimental XRD patterns (black circles) are shown in comparison with the calculated profiles (red and blue

 doi:10.20944/preprints202603.1041.v1

lines, respectively). Short vertical bars on the top and bottom panels indicate positions of Bragg's maxima in the monoclinic $P2_1/n$ and tetragonal $I4_1/amd$ structures, respectively. Insets shows polyhedral views of monazite-type $LaVO_4$:Bi and zircon-type $Y_{0.5}Lu_{0.5}VO_4$:Bi structures. Reproduced with permission from Ref. [34] under Creative Commons CC BY license.

3.2. Morphology of Luminescent $REVO_4$ Materials

The development of modern optoelectronic devices strongly depends on the advancement of luminescent materials with improved characteristics. These materials must exhibit specific functional properties, such as brightness, resolution, spectral energy distribution and lifetime under practical operating conditions. Such properties are determined by the structural and morphological features of the material used. Depending on the intended application, synthesized luminescent $REVO_4$ materials should possess precisely defined functional characteristics. Among them, uniform particle size distribution, spherical morphology without agglomeration are particularly critical [35,36].

Precise control over nanoparticle size, uniformity, distribution and surface area enable significant enhancement of optical properties, such as lifetimes of intermediate energy levels, dopant ion emission at specific wavelengths, and reduction of light scattering when particle dimensions are smaller than the wavelength of incident light. Luminescent materials at the nanoscale are especially important because they bridge the gap between molecular and micron scales, offering unique opportunities for advanced applications. Their effectiveness arises from a high surface-to-volume ratio, which ensures that a large fraction of atoms remain available for interaction with surrounding molecules [37].

Furthermore, the small particle size provides greater flexibility for manipulation and facilitates efficient doping with activator ions. Since many dopant ions are located near particle surfaces in asymmetric crystalline environments, their emission behaviour differs from that of ions in regular crystallographic positions. This distinction opens pathways to novel and tuneable optical effects, positioning nanostructured luminescent materials as a promising frontier in optoelectronics [38].

As mentioned above, the morphology of $REVO_4$ is strongly influenced by the preparation method and reaction parameters, such as reaction temperature, pressure, concentration of precursor solutions, pH value, kind of solvent, aging time, molar ratio of RE^{3+}/V^{5+}, the addition of surfactant and different dopant ions.

The $GdVO_4$:Eu^{3+}/Sm^{3+} and $GdVO_4$:Ho^{3+}/Yb^{3+} obtained with solid state reaction synthesis show that the powders contain chunks with irregular spheres with an average diameter in range from 1 μm to 8 μm [19,39].

Using sol-gel route, the $GdVO_4$ nanomaterial can be synthesized using different carboxylic acids, resulting in a homogeneous distribution of spherical particles with average sizes ranging from 50 to 100 nm [40]. In another approach, a tartaric acid–assisted sol–gel method was employed, where tartaric acid acted simultaneously as a chelating agent and as an additional fuel during precursor combustion. Key synthesis parameters, such as calcination temperature and the molar ratio between total metal ions and tartaric acid, directly influence the particle size and crystallinity of the final product, consisting of spherical nanoparticles with diameters between 20 and 30 nm [26].

$GdVO_4$ nano- and microcrystals with diverse morphologies and sizes were successfully synthesized using hydrothermal process and trisodium citrate (Na_3Cit) as the chelating ligand. By employing $Gd(NO_3)_3$ and Na_3VO_4 as precursor together with Na_3Cit in varying molar ratios relative to Gd^{3+} ions, different morphologies and particle sizes were obtained. For instance, when the molar ratio of Na_3Cit to Gd^{3+} was 4:1, uniform pancake-like microstructures were produced, with an average thickness of 200 nm and a diameter of approximately of 1 μm [22]. In another approach, hydrothermal synthesis under varying pH conditions, reaction media and reaction times yielded Eu^{3+}-doped $GdVO_4$ phosphors with a wide range of morphologies as rhombic, spherical, and cubic structures, as well as irregular short nanorods [21]. Applying various reaction components, such as EDTA-Na_2 and EDTA, and adjusting the pH of the solution, the hydrothermal method allows to tune the shape of $GdVO_4$ into short and long nanowires and nanorods, nanoparticles and spheres [41]

 doi:10.20944/preprints202603.1041.v1

Both as-prepared $GdVO_4$:Ho^{3+}/Yb^{3+} samples and those re-heated at 300 °C , synthesized by the co-precipitation method, reveal bundles composed of 5–6 individual nanorods, each approximately 5 nm in diameter and up to 20 nm in length, aligned in different orientations. When the same samples were annealed at 600 °C, the nanorods transformed into single ellipsoidal particles with an average size of about 20 nm, while at higher annealing temperatures of 800 °C and 1000 °C, the morphology changed further, yielding irregular spherical particles of approximately 100 nm in size along with elongated rod-like structures [13].

The YVO_4 nanoparticles synthesized using a simple microwave irradiation processing exhibited a size was in the range of 5–18 nm, which was extremely dependent on the pH value of the solution [42]. On other side, the YVO_4:Bi^{3+}: Eu^{3+} materials synthesized by microwave and ultrasonic radiation-activated technique have a pronounced spherical shape with a predominant diameter in the range of 20-40 nm [43].

As a further example, SEM and TEM imagesof MVO_4/g-C_3N_4 (M = La, Gd) prepared by the hydrothermal method are given in Figure 3. The pure g-C_3N_4 exhibits a nanosheet structure with a smooth surface (Figure 3a), while pure $GdVO_4$ powders display a coral-like morphology (Figure 3b). The TEM image of the $GdVO_4$/g-C_3N_4 composite (Figure 3c) reveals two distinct components: the black coral-like structures corresponding to $GdVO_4$, and the French-grey sheet-like structures belonging to g-C_3N_4. On the other hand, pure $LaVO_4$ demonstrates a pin-like nanostructure (Figure 3d). Figures 3e and 3f illustrate the $LaVO_4$/g-C_3N_4 composite, where both $LaVO_4$ and g-C_3N_4 are clearly distinguishable, with $LaVO_4$ particles well adhered to the g-C_3N_4 surface. Thus, the constitution of MVO_4/g-C_3N_4 (M = La, Gd) composites is readily identifiable, which facilitates efficient charge carrier transport compared to pure MVO_4 (M = La, Gd) [44].

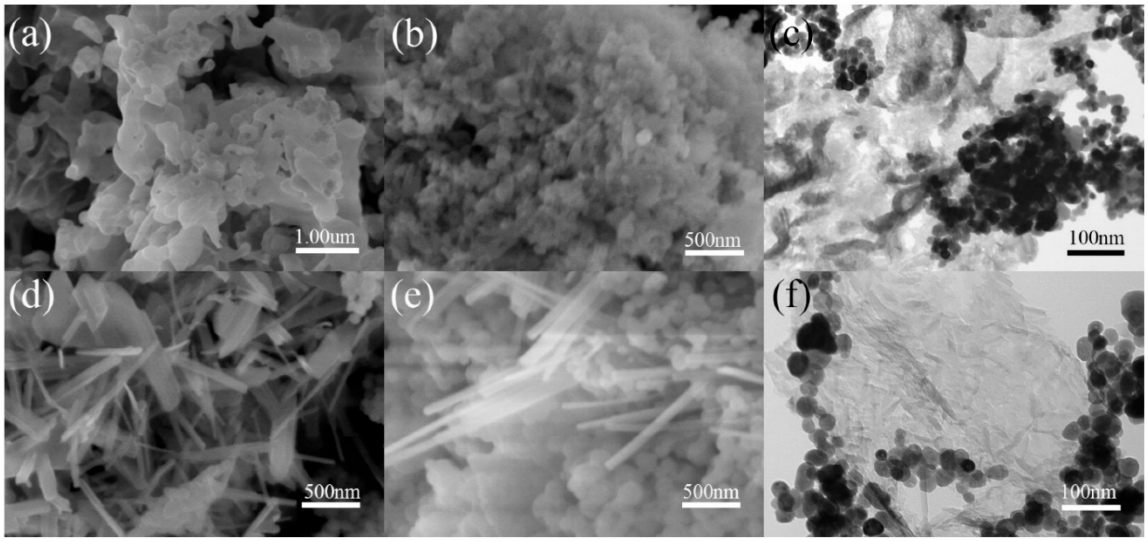

Figure 3. The SEM images of (a) g-C_3N_4, (b) $GdVO_4$, (d) $LaVO_4$, and (e) $LaVO_4$/g-C_3N_4 and the TEM images of (c) $GdVO_4$/g-C_3N_4 and (f) $LaVO_4$/g-C_3N_4. Reproduced with permission from Ref. [44] under Creative Commons CC BY license.

4. Discussion

4.1. Optical Properties of $REVO_4$ Materials

The lanthanides (Ln), spanning lanthanum (Z = 57) to lutetium (Z = 71), have a general electronic configuration of [Xe]$6s^2 5d^1 4f^n$. Typically, the 5d electron shifts into the 4f shell, giving $4f^{n+1}$, though exceptions exist (e.g., Gd). As atomic number increases, the 4f orbitals contract inward, a phenomenon called the lanthanide contraction making them to behave like inner electrons and limiting their role in bonding. This results in similar chemical properties across the series, dominated by outer valence electrons. Upon ionization, lanthanides form stable +3 ions ([Xe]$4f^n$), with $5s^2 5p^6$

 doi:10.20944/preprints202603.1041.v1

orbitals shielding the 4f electrons, so crystal field effects remain weak and are treated with perturbation theory [45]. Inorganic materials doped with Ln^{3+} are essential across numerous fields, owing to their wide-ranging applications: LED diodes, luminescent monitors/electromagnetic displays, lasers, thin-film phosphors, drug delivery systems, luminescence thermometry, chemical sensing, biosensing, infrared fluorescence bioimaging, photothermal therapy, gas sensing, anti-counterfeiting technologies and so on.

$REVO_4$ (RE = Gd, Y and Lu) are widely recognized as excellent host materials for various dopant ions, owing to their ability to be efficiently excited by UV radiation and their favourable charge-transfer energy. Because charge transfer from vanadate groups to optically active trivalent lanthanide ions (Ln^{3+}) is highly efficient, luminescence can be achieved even at extremely low dopant concentrations [46].

In terms of luminescence mode, the $ReVO_4$ doped with one of Ln^{3+} = Eu^{3+}, Dy^{3+} or Sm^{3+} ions can act as downconversion luminescent sensing materials, while double or triple doped with combinations of Ln^{3+} ions such as Er^{3+}/Yb^{3+}, Ho^{3+}/Yb^{3+}, Tm^{3+}/Yb^{3+}, or $Er^{3+}/Tm^{3+}/Ho^{3+}/Yb^{3+}$ ions, act as an upconversion luminescent sensing materials, producing a wide range of emission colours. Also, VO_4 can be doped with Nd^{3+} for additional sensing applications [47,48].

4.1.1. Downconversion $REVO_4$-Based Luminescent Materials and Sensing Applications

Stokes luminescence, also known as downconversion (DC), is a process in which matter absorbs photons of higher energy and re-emits photons of lower energy. DC luminescence follows Stokes' law, describing the conversion of high-energy excitation into lower-energy emission [49].

As an example for $REVO_4$-based DC-luminescent materials, the schematic diagram of the energy transfer process in $GdVO_4$:Tb samples is given in Figure 4. The $VO_4^{3-} \rightarrow Tb^3$ one-electron charge transfer takes place between the 2p orbital of oxygen (O^{2-}) and the vacant 3d orbital of the central vanadium (V^{5+}) in the tetrahedral VO_4^{3-} with Td symmetry. According to the molecular orbital theory, energy levels involved are the ground $^1A_1$ state and the excited $^1T_1$, $^1T_2$, $^3T_1$ and $^3T_2$ states. These transitions from $^1A_1$ level to the $^1T_1$ and $^1T_2$ generate a broad and intense charge-transfer absorption band in the UV region [11]. At the same time, weak absorption features indicate a low-efficiency reverse transfer process from Tb^{3+} to VO_4^{3-}. There are four possible energy transfer (ET) pathways: ET_1 ($Gd^{3+} \rightarrow VO_4^{3-}$), ET_2 ($VO_4^{3-} \rightarrow Tb^{3+}$), ET_3 ($Tb^{3+} \rightarrow VO_4^{3-}$, weak) and ET_4 ($Gd^{3+} \rightarrow VO_4^{3-} \rightarrow Tb^{3+}$) which demonstrate cooperative interactions among Gd^{3+}, VO_4^{3-} and Tb^{3+} ions. Overall, $VO_4^{3-} \rightarrow Tb^{3+}$ transfer was identified as the dominant process, supported by spectral shifts, broadened emission bands, and lifetime analysis [50].

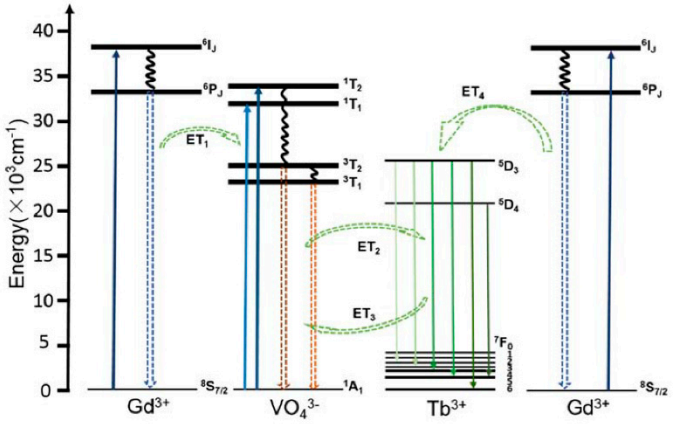

Figure 4. Schematic diagram of the energy transfer process in $GdVO_4$:Tb samples. Reproduced with permission from Ref. [50] under Creative Commons CC BY license.

Eu^{3+} and Bi^{3+} ions co-doped $LuVO_4$ thin films annealed at 1000 °C exhibit pronounced luminescent behaviour. The Eu^{3+} ions generate intense red emission via the $^5D_0 \rightarrow {}^7F_2$ transition with a

 doi:10.20944/preprints202603.1041.v1

similar feature as the $GdVO_4:Eu^{3+}$ samples obtained by coprecipitation synthesis and additionally annealed at 1000°C [51]. As an example, excitation and emission spectra of $LuVO_4:Eu^{3+},Bi^{3+}$ films are given in Figure 5.

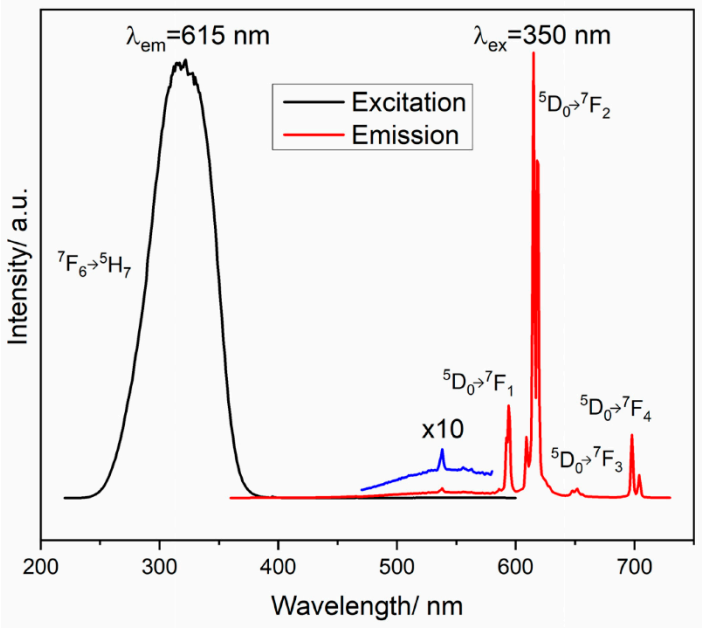

Figure 5. Excitation and emission spectra of $LuVO_4$ films with 2.5 at. % Eu^{3+} and 1.5 at. % Bi^{3+} after 3 h of annealing at 1000 °C. Reproduced with permission from Ref. [52] under Creative Commons CC BY license.

Under 350 nm excitation, emission peaks at 594, 615, 650, and 700 nm are produced, corresponding to Eu^{3+} transitions $^5D_0 \rightarrow {}^7F_J$ (J = 1, 2, 3, 4), while the most prominent emission is observed at 615 nm. The Bi^{3+} ions act as sensitizers by absorbing UV radiation and transferring the energy to Eu^{3+} ions. The characteristic Bi^{3+} emission band at 550 nm is significantly reduced in co-doped samples, confirming efficient $Bi^{3+} \rightarrow Eu^{3+}$ energy transfer. $LuVO_4$ thin films exhibit stable and tuneable luminescence, making them highly promising for optoelectronic applications such as displays and light emitters, as well as efficient phosphors for LEDs, particularly in warm-white lighting. Their properties also open opportunities in optical sensing and biological imaging, where reliable luminescence performance is essential [52]. Analysis of the intensity ratio R = $I(^5D_0 \rightarrow {}^7F_2)/I(^5D_0 \rightarrow {}^7F_1)$ demonstrates that Bi^{3+} promotes Eu^{3+} occupation at lower-symmetry sites. According to Dexter's theory, quadrupole–quadrupole interactions dominate the transfer mechanism, consistent with other $Bi^{3+} \rightarrow Eu^{3+}$ systems [53].

The Eu^{3+} ions are frequently employed as luminescent activators for bioapplications (biodetection, bioimaging and biosensing) and chemical sensing due to their unique luminescence properties. Due to the different crystal field surroundings, the Eu^{3+} ions situated at multiple sites in different materials exhibit distinct photoluminescent spectra and photoluminescent decays. The long-lived luminescence of Eu^{3+} ions is highly advantageous for background-free, time-resolved photoluminescence biodetection. The Eu^{3+}-activated nanomaterials have demonstrated broad applicability in both heterogeneous and homogeneous biodetection, *in vitro* and *in vivo* bioimaging, anti-aging antibacterial, anti-cancer and antioxidant effects [54,55]. The $GdVO_4:Eu^{3+}$ nanoparticles are excellent candidates for multifunctional material development, as they can perform diverse and polyvalent functions.

The redox-active $GdVO_4:Eu^{3+}$ and $LaVO_4:Eu^{3+}$ nanoparticles can intensify damage in oxidatively stressed L929 cells, even at concentrations that remain non-toxic to normal cells. This effect is linked to the internalization of the nanoparticles and is mediated through activation of the intrinsic mitochondrial apoptotic pathway, excessive reactive oxygen species (ROS) generation and Ca^{2+}

 doi:10.20944/preprints202603.1041.v1

signaling. These results highlight the potential of $GdVO_4:Eu^{3+}$ and $LaVO_4:Eu^{3+}$ nanoparticles as promising candidates for using as anti-cancer agents, as depicted in Figure 6 [56].

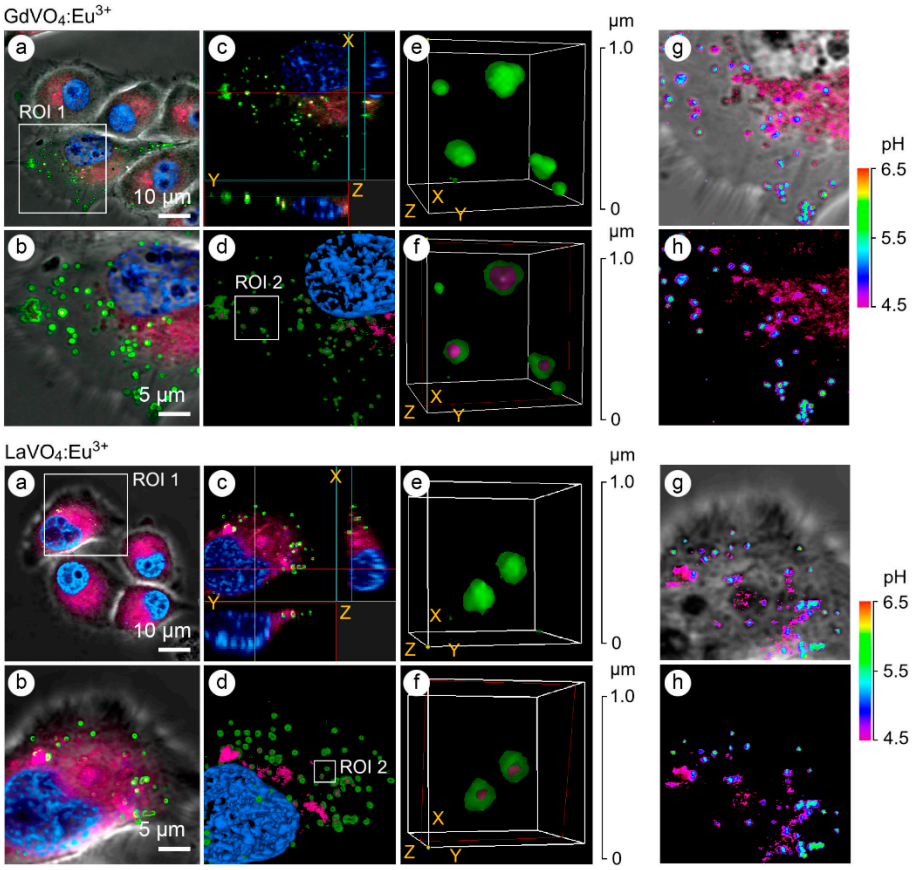

Figure 6. Representative LSCM images of the endosome-positive L929 cells following treatment with $GdVO_4Eu^{3+}$ and $LaVO_4Eu^{3+}$ nanoparticles at 20 mg/L for 1 h. The L929 cells were transfected with GFP-Rab5a/GFP-Rab7a and, 24 h after transfection, the cells were exposed to the investigated NPs. The Rab5a and Rab7a proteins were markers of the early and late endosomes, respectively. The GFP-Rab5a/GFP-Rab7a-positive endosomes (green) and NPs' autofluorescence signals (magenta) were detected. The cell nuclei are shown in blue (DAPI staining). Single-optic section phase contrast and fluorescence-merged imaging (Panel (a)); magnified single-optic section fluorescence imaging of the ROI1 (Panel (b)); orthogonal XZ and YZ projections of the ROI1 (Panel (c)); 3D reconstruction of the ROI1 (Panel (d)); complete 3D reconstruction of the endosomes without and with the NPs' fluorescence channel (magenta) of the ROI2 (Panel (e)); cross section of the endosomes (red frame) demonstrating the intra-endosomal localization of the NPs (magenta) of the ROI2 (Panel (f)); and pseudocolored and phase-contrast imaging of the endosomal pH using the LysoSensor ratiometric probe (molecular probes, L22460) of the ROI1 (Panels (g,h)). Ratiometric pseudocolored images were constructed from two emission images at 450 ± 33 nm and 510 ± 20 nm, respectively. Both were excited at 365 ± 8 nm. The cells were preliminarily exposed to pH calibration buffers (pH 4.5–6.5). Reproduced with permission from Ref. [56] under Creative Commons CC BY license.

A ^{64}Cu-labeled multifunctional nanoprobe targeting integrin $\alpha_2\beta_1$ (often used as metastasis suppressor) was developed using $GdVO_4:Eu^{3+}$ two-dimensional tetragonal nanosheets for in vitro fluorescence studies, in vivo magnetic resonance imaging (MRI) and micro- positron emission tomography (PET) imaging of prostate cancer. The unique water solubility and biocompatibility make $GdVO_4:Eu^{3+}$ highly versatile for biomedical applications [57] and with strong potential as radionuclide carrier and as contrast agents for theranostic applications [58,59].

Due to their negative surface potential, $GdVO_4:Eu^{3+}$ nanoparticles strongly adsorb metal cations. Among common blood ions, Cu^{2+} uniquely induces distinct fluorescence quenching. $GdVO_4:Eu^{3+}$

 doi:10.20944/preprints202603.1041.v1

nanoparticles are promising magnetic/fluorescent multimodal probes for Cu^{2+} ions detection in blood [60]. Colloidal $GdVO_4:Eu^{3+}@SiO_2$ nanocrystals could find a promising application for highly selective and sensitive detection of Cu^{2+} ions in an environmental or biological sample [61]. Also, Eu^{3+}activated ultra-small nanoparticles ($EuVO_4$ and $GdVO_4:Eu^{3+}$) could potentially be used for the detection of pesticides in environmental and biomedical fields, due to photoluminescence quenching [62]. Hydrogen peroxide (H_2O_2) acts as a strong quencher of ultra-small (2-3 nm) $GdVO_4:Eu^{3+}$ fluorescence. The observed Eu^{3+} luminescence quenching is found to be more effective with increasing concentration of H_2O_2.To evaluate selectivity for H_2O_2, several potentially interfering ions were also tested. Common physiological ions such as Ca^{2+}, Zn^{2+} and Mg^{2+} did not affect fluorescence intensity, while Cu^{2+} and Fe^{3+} quenched even more efficiently than H_2O_2 [63]. Two primary mechanisms were identified as responsible for the quenching of Eu^{3+} luminescence in $GdVO_4:Eu^{3+}$ nanoparticles: i) reduction in the efficiency of non-radiative resonance energy transfer from the vanadate groups to Eu^{3+} ions, caused by scattering effects introduced by V^{4+} ions; ii) direct luminescence quenching of Eu^{3+} ions by –OH groups formed on the nanoparticle surface as a result of H_2O_2 decomposition [64].

The additional sensing application and distribution of $Gd_{0.6}Eu_{0.4}VO_4$ nanoparticles was investigated with XRF spectroscopy after injection of their colloidal solutions into mouse ear pinnae. The distribution of the nanoparticles was mapped by raster scanning the sample and detecting the V K_α, Gd L_α, and Eu L_α fluorescence emissions. It was found that all three elements coexist and therefore no short-term out-diffusion of those elements from the nanoparticles to the tissues takes place. These results provided a proof-of-concept that XRF mapping and spectroscopy are excellent tools for the determination of the long-term fate of $Gd_{0.6}Eu_{0.4}VO_4$ nanoparticles in tissue in terms of element leaching and stability for diagnostic and therapeutic purposes [65].

4.1.2. Upconversion $REVO_4$-Based Luminescent Materials and Sensing Applications

Upconversion (UC) luminescence is a non-linear anti-Stokes process with low energy excitation light (NIR region). In recent years, UC materials excited by NIR light illumination and emitting in visible (Vis) region have received much attention. Typically, UC materials are composed of a host material with low phonon energy, such as $REVO_4$, and sensitizer ions (commonly Yb^{3+}) along with activator ions (most often Er^{3+}, Tm^{3+}, or Ho^{3+}, or their combination). Yb^{3+}-sensitized UC materials are typically excited at 980 nm. The Yb^{3+} ion possesses a simple energy structure with only two states: the ground state ($^2F_{7/2}$) and the excited state ($^2F_{5/2}$), separated by an energy gap of approximately 10,000 cm^{-1}. Yb^{3+} acts as the sensitizer due to its strong absorption cross-section at 980 nm and efficient energy transfer to Er^{3+}, while Er^{3+} provides the emission. Importantly, Yb^{3+} absorbs in the NIR region where inexpensive laser diodes operate efficiently. This absorption enhances luminescence efficiency by transferring excitation energy to Er^{3+}, Ho^{3+}, or Tm^{3+} ions [66].

The intensity of upconversion emissions is strongly influenced by several factors, including temperature, particle morphology, surface characteristics, and concentration ratio between dopant ions (Er^{3+}, Ho^{3+}, Tm^{3+}) and sensitizer ions (Yb^{3+}). In the $GdVO_4$ host matrix, varying the concentration ratio of Yb^{3+} to Er^{3+} alters the balance between green and red emissions. It is important to note that literature indicates only a few Er^{3+} or Yb^{3+}/Er^{3+}-doped inorganic UC materials which emit intense green emission under NIR excitation. Specifically, increasing the Er^{3+} concentration enhances the green emission in doped-$GdVO_4$ and YVO_4 materials. This effect can be attributed to perturbations in site symmetry, which promote stronger emission from the $^2H_{11/2}$ state. The perturbation arises from the hypersensitive nature of the $^2H_{11/2}$ state and the difference in ionic radii between Yb^{3+} and Gd^{3+} ions, leading to modified local environments that favour enhanced luminescence [67,68]. The UC mechanism involves Yb^{3+} absorbing most of the excitation energy and transferring it to Er^{3+}, whose long-lived excited states enable multiphoton absorption and radiative relaxation, producing green and red emissions. Nanoparticles show weaker UC intensity compared to bulk material, though the emission band shapes and green-to-red ratios remain unchanged [69].

Figure 7 demonstrates how excitation wavelength and elemental composition influence the green UC emission intensity of YVO_4 nanomaterials. Excitation at 785 nm produces stronger UC

 doi:10.20944/preprints202603.1041.v1

emission in YVO_4:Er^{3+} compared to YVO_4:Er^{3+},Yb^{3+} due to Er^{3+}→Yb^{3+} back energy transfer, which reduces Er^{3+} UC emission by channeling energy into Yb^{3+} relaxation. In contrast, the most intense green UC luminescence is observed in YVO_4:Er^{3+},Yb^{3+} under 975 nm excitation due to the large absorption cross-section of Yb^{3+} ions ($^2F_{7/2} \rightarrow {}^2F_{5/2}$ transition) and efficient energy transfer to Er^{3+} ions [70]. Also, the laser pump power can affect the intensity of the Er^{3+} emission measured for large nanoparticle ensembles and single particle in the YVO_4:Yb,Er system [71].

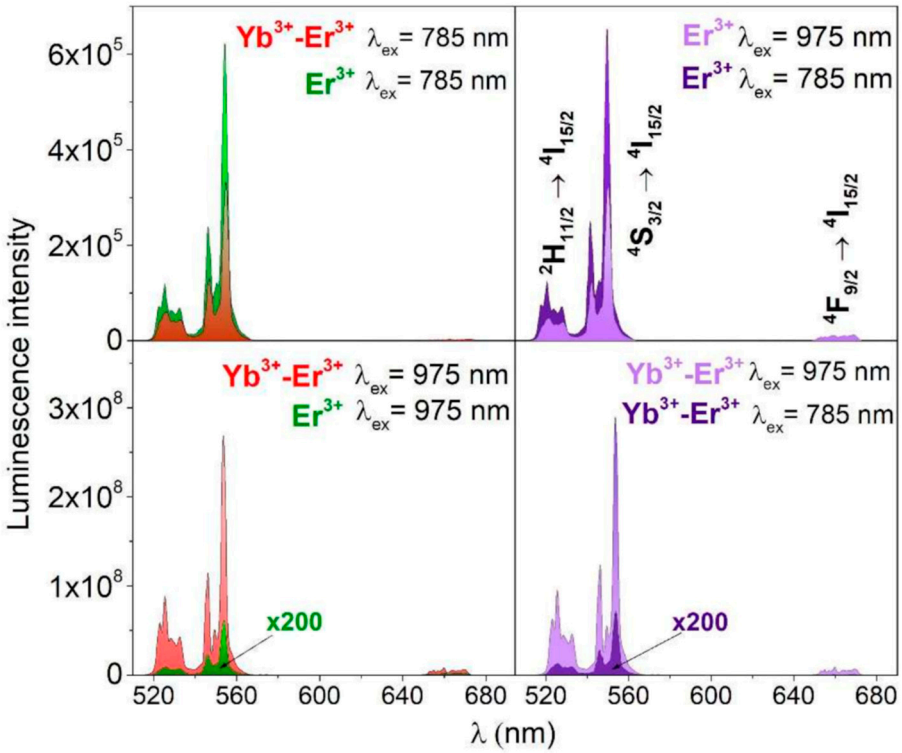

Figure 7. Non-normalized UC emission spectra of the obtained nanomaterials YVO_4: Er^{3+} and YVO_4: Yb^{3+}, Er^{3+} under λ_{ex} = 785 or 975 nm (≈50 W/cm²). Reproduced with permission from Ref. [70] under Creative Commons Attribution (CC BY) license.

The incorporation of Ho^{3+} ions into the matrix, together with Yb^{3+} ions, is particularly effective due to the favourable energy level distribution of Ho^{3+} ions. Radiative transitions from the $^5S_2/^5F_4$ level of Ho^{3+} to the ground state ($^5I_8$) produce green emission around 545 nm, while transitions from the $^5F_5$ level to $^5I_8$ yield red emission near 650 nm under UV and NIR excitation, respectively. The intensity of red UC emission originating from the $^5F_5 \rightarrow {}^5I_8$ transition of Ho^{3+} increases consistently with higher Yb^{3+} concentrations. Typically, strong red UC emission in Ho^{3+}/Yb^{3+} systems requires relatively high Ho^{3+} concentrations, explained by cross-relaxation processes between Ho^{3+} energy levels that suppress green emission [72,73].

$GdVO_4$:Tm^{3+},Yb^{3+} material, under 980 nm excitation, exhibits UC luminescence in three distinct regions: a dominant blue emission at 475 nm arising from the $^1G_4 \rightarrow {}^3H_6$ transition of Tm^{3+}ions, a weaker red emission at 650 nm attributed to the $^1G_4 \rightarrow {}^3F_4$ transition and an infrared emission at 808 nm corresponding to the $^3H_4 \rightarrow {}^3H_6$ transition of Tm^{3+} ions [74]. Figure 8 summarizes the structure and luminescence behavior of Tm^{3+},Yb^{3+}:$GdVO_4$@SiO_2 core–shell nanoparticles, which can serve as biolabels in the visible range and luminescence thermometers within the first biological window (I-BW) (Figure 8a). Under 980 nm excitation, the UC emission spectra reveal that most bands decrease in intensity with rising temperature, except the 700 nm band, which slightly increases (Figure 8b). The energy transfer mechanism (Figure 8c) involves sequential absorption by Yb^{3+} ions ($^2F_{7/2} \rightarrow {}^2F_{5/2}$) and transfer to Tm^{3+} levels, ultimately populating $^1G_4$ and producing blue (475 nm) and red (650 nm) emissions, while transitions from $^3F_3$ and $^3H_4$ yield emissions at 700 nm and 800 nm. Non-radiative

 doi:10.20944/preprints202603.1041.v1

relaxation, Tm–Tm cross-relaxation and efficient population of the $^3H_4$ level can explain the strong NIR emission observed at 800 nm and the temperature-dependent spectral behavior [75].

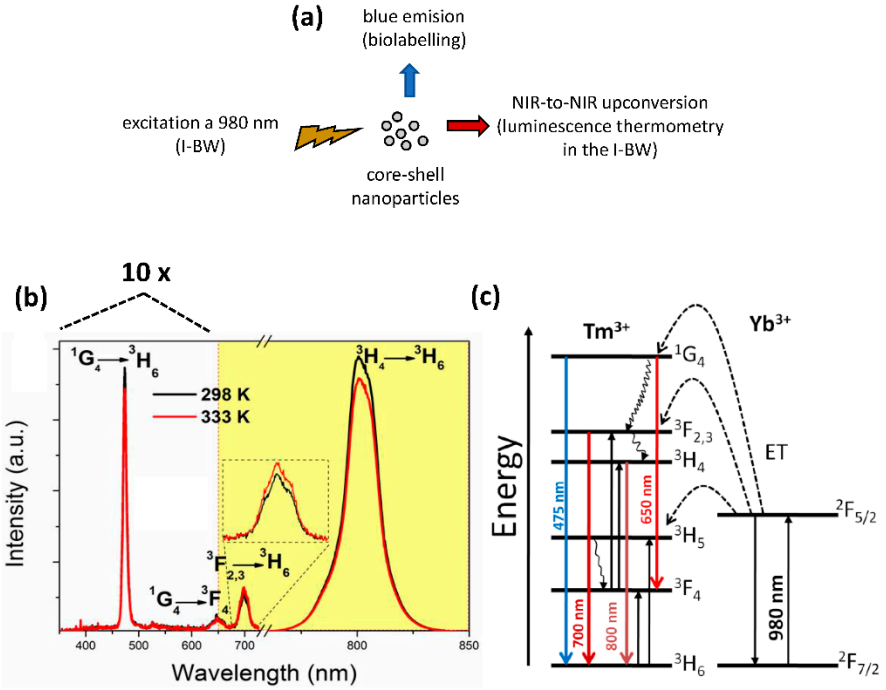

Figure 8. (a) Schematic representation of the pumping and emission bands generated by the Tm,Yb:$GdVO_4$@SiO_2 core-shell nanoparticles, (b) Upconversion emission spectra of the Tm,Yb:$GdVO_4$@SiO_2 core-shell nanoparticles at room temperature and at 333 K. The inset shows the magnification of the peak located at 700 nm, (c) Energy level diagram of $Tm^{3+}$and Yb^{3+} ions in $GdVO_4$, indicating the absorption, energy transfer and emission pathways. Reproduced with permission from Ref. [71] under Creative Commons Attribution (CC BY) license.

It is common to use a 980 nm excitation source for UC emission, but this wavelength has drawbacks in biomedical applications, including strong water absorption, limited tissue penetration and local heating that can damage cells. To overcome these issues, research has shifted toward shorter excitation wavelengths, particularly 808 nm, which lies within the biological NIR windows (650–950 and 1100-1750 nm) where tissues are more transparent. The second NIR window is especially attractive for fluorescence imaging due to deeper penetration, higher resolution, and reduced scattering. At 808 nm, water absorption is lower, penetration is deeper, and heating effects are minimized [76,77]. The excitation wavelength shift is possible Yb^{3+} ions with Nd^{3+} ions, which have a strong absorption band centered at 808 nm. UC emission spectra of $GdVO_4$:Nd^{3+}/Er^{3+} and $GdVO_4$:Nd^{3+}/Ho^{3+} systems under 808 nm excitation show three bands: green emission (520–565 nm, max ~540 nm), red emission (570–630 nm, max ~597 nm), and another red band (640–680 nm, max ~675 nm).The dominant red emission at 597 nm corresponds to the Nd^{3+} ($^4G_{7/2} \rightarrow {}^4I_{11/2}$) transition, while the other bands arise from Er^{3+} and Ho^{3+} transitions [48]. $GdVO_4$ single crystals doped with Nd^{3+} ions under 808 nm continuous-wave laser excitation across varying temperatures have been studied for optical thermometry. The excitation pathway involves ground-state absorption, non-radiative relaxation, excited-state absorption and energy-transfer upconversion, which enhances higher-level populations. As temperature increases, phonon-assisted processes such as cross relaxation and non-radiative transitions become more efficient, leading to dramatic emission intensity enhancements at 400 °C compared to room temperature [78]. YVO_4:Nd^{3+}nanophosphors can also be used as NIR-to-NIR thermal sensors in a wide temperature range [79]. Ultra-small stoichiometric $NdVO_4$ nanoparticles (3-4 nm) dispersed in water exhibit long-term stability, large absorption cross-sections at 808 nm, and excellent biocompatibility, making them promising

 doi:10.20944/preprints202603.1041.v1

multifunctional agents for biomedical imaging and *in vivo* photothermal cancer therapy using a mouse model. A concentrated colloidal dispersion of $NdVO_4$ nanoparticles in Tris-buffered saline (TBS) was subcutaneously injected, and infrared fluorescence imaging with an InGaAs CCD camera enabled precise localization of the injection site [80,81].

Due to the unique 4f-electron structure of lanthanide ions, UC nanomaterials have been widely investigated for biomedical and materials science sensing applications. Due to remarkable optical, electronic and magnetic properties, these materials can be used in biomedicine, luminescence imaging, cell labeling probe, magnetic resonance imaging (MRI), photodynamic therapy (PDT), chemotherapy, single-photon emission computed tomography (SPECT), X-ray computed tomography(CT), optical biosensing/biodetection, and many other sensing technologies. In biomedical contexts, UC nanoparticles offer several advantages: deeper penetration into biological tissues, minimal autofluorescence background, reduced scattering and absorption, excellent photostability and negligible photoblinking [82,83].

The unique ability of UC nanoparticles to function as MRI contrast agents, coupled with their strong tissue penetration and prolonged circulation, enables highly sensitive imaging of biological targets. Beyond diagnostics, these nanoparticles can be precisely engineered in size and morphology to act as multifunctional platforms, supporting both imaging and therapeutic applications such as photodynamic therapy, photothermal therapy, and chemotherapy. Their luminescent responsiveness to temperature further broadens their utility, making them valuable tools for thermometry and sensor development. Altogether, UC nanoparticles represent versatile systems at the intersection of medical innovation and opto-electronic technology [84,85].

The $YVO_4:Er^{3+},Eu^{3+},Yb^{3+}$ nanoparticles with an average size of ~100 nm, synthesized using melamine formaldehyde as a template, can serve as dual-mode excitation materials for bioimaging and have been successfully applied *in vitro* for imaging HeLa cells. Cytotoxicity was evaluated using the methyl thiazolyl tetrazolium (MTT) assay, confirming that functionalized YVO particles exhibit low cytotoxicity, supporting their potential biomedical applications [86]. $GdVO_4@SiO_2$:Tm,Yb core–shell structures demonstrate excellent thermal sensitivity and resolution, making them suitable as intracellular thermal probes for measuring temperature within living HeLa cells [75].

$YVO_4:Nd^{3+}$ nanoparticles have emerged as multifunctional nanotheranostic agents, enabling fluorescence imaging, magnetic resonance imaging, and enhanced sonodynamic therapy of orthotopic gliomas. Similarly, $GdVO_4:Nd^{3+}$ particles are promising candidates for time-gated bioimaging [87–89]. Figure 9 illustrates *in vitro* imaging studies of $YVO_4:Er^{3+}/Yb^{3+}$ UC-MHNSPs, highlighting their permeability and translocation in HeLa cell lines [90].

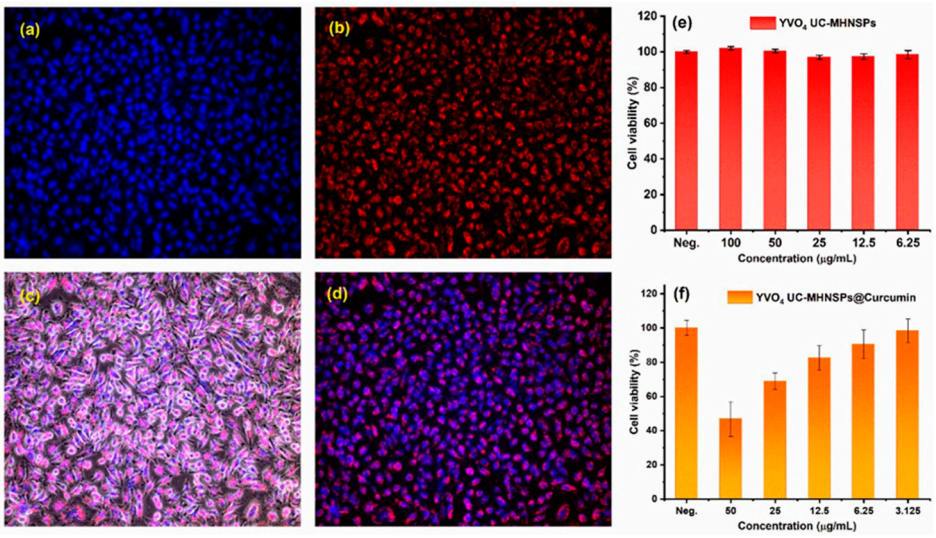

Figure 9. In vitro fluorescence images of $YVO_4:Er^{3+}/Yb^{3+}$ UC-MHNSPs uptake by HeLa cell lines, (a) nuclear stain (Hoechst 33342), (b) red emission from $YVO_4:Er^{3+}/Yb^{3+}$ UC-MHNSPs, (c,d) merged fluorescence bright-field and

 doi:10.20944/preprints202603.1041.v1

dark-field pictures of HeLa cells under 980 nm excitation. (e) Cell viability assessed by CCK-8 assay after incubating with various quantities of $YVO_4:Er^{3+}/Yb^{3+}$ UC-MHNSPs for 24 h and (f) antitumor activity of $YVO_4:Er^{3+}/Yb^{3+}$ UC-MHNSPs after conjugation with different quantities of curcumin. Reproduced with permission from Ref. [90] under Creative Commons Attribution (CC BY) license.

The $REVO_4$ UC nanomaterials have been studied as sensors for luminescence thermometry. Temperature monitoring can be achieved by remotely detecting changes in nanomaterials luminescent properties offering valuable their applications in biomedicine, micro/nanoelectronics and integrated photonics [91]. Temperature sensing with UC nanoaparticles is of particular interest for biomedicine, because the excitation typically occurs in the NIR spectral region, and autofluorescence from biological material does not affect the measurements. In this context, $GdVO_4:Er^{3+}/Yb^{3+}$ and $YVO_4:Ho^{3+}/Yb^{3+}$ nanoparticles have been investigated for temperature sensing, with their upconversion emission spectra recorded across the range of 307-473 K and 12–300 K, respectively [69,92]. Figure 10(a) presents the emission spectra of YVO_4:1%Er^{3+} in the temperature range 300–800 K together with temperature dependence of the fluorescence intensity ratio (FIR) between the emission peaks at 525 nm ($^2H_{11/2}$–$^4I_{15/2}$) and 553 nm ($^4S_{3/2}$–$^4I_{15/2}$) [93]. Because two closely separated levels show Boltzmann-type relative population, the integrated FIR of transitions from the $^2H_{11/2}$ and $^4S_{3/2}$ levels to the ground level $^4I_{15/2}$ can be approximated using Boltzmann distribution as follows [94]:

$$FIR = \frac{I(^2H_{11/2} \rightarrow ^4 I_{15/2})}{I(^4S_{3/2} \rightarrow ^4 I_{15/2})} = \frac{g_H A_H h\nu_H}{g_S A_S h\nu_S} \exp\left(-\frac{\Delta E}{kT}\right) = \mathrm{B} \exp\left(-\frac{\Delta E}{kT}\right) \quad (1)$$

where $\boldsymbol{g_H}$ and $\boldsymbol{g_S}$ are the degeneracies of the $^2H_{11/2}$ and $^4S_{3/2}$ levels, respectively; $\boldsymbol{A_H}$and $\boldsymbol{A_S}$, $\boldsymbol{\nu_H}$ and $\boldsymbol{\nu_S}$ are the spontaneous emission rates and frequencies of the $^2H_{11/2} \rightarrow ^4I_{15/2}$ and $^4S_{3/2} \rightarrow ^4I_{15/2}$ transitions, respectively; h is the Planck's constant; k is the Boltzmann's constant; and T is the absolute temperature. Equation (1) can be expressed as follows:

$$\ln(FIR) = ln(\mathrm{B}) + \left(-\frac{\Delta E}{kT}\right) = ln(\mathrm{B}) + \left(-\frac{C}{T}\right) \quad (2)$$

where B and C are the constants that need to be determined. Fitting the experimental data with Equation (2) demonstrates a strong correlation between theory and experiment, consistent with previous reports on thermometry based on Er^{3+} UC emission [94,95]. The relative sensor sensitivity, S_r [in $\%K^{-1}$] of the luminescent probe, is defined as relative change in the FIR with temperature (Figure 10(b)):

$$S_r = \frac{1}{FIR}\frac{\Delta FIR}{\Delta T} \times 100\% \quad (3)$$

The highest relative sensitivity was achieved for a dual layered $YVO_4:Eu^{3+}/YVO_4$: Dy^{3+} sample, exhibiting a maximum sensitivity of 3.6% K^{-1} at 640 K [93].

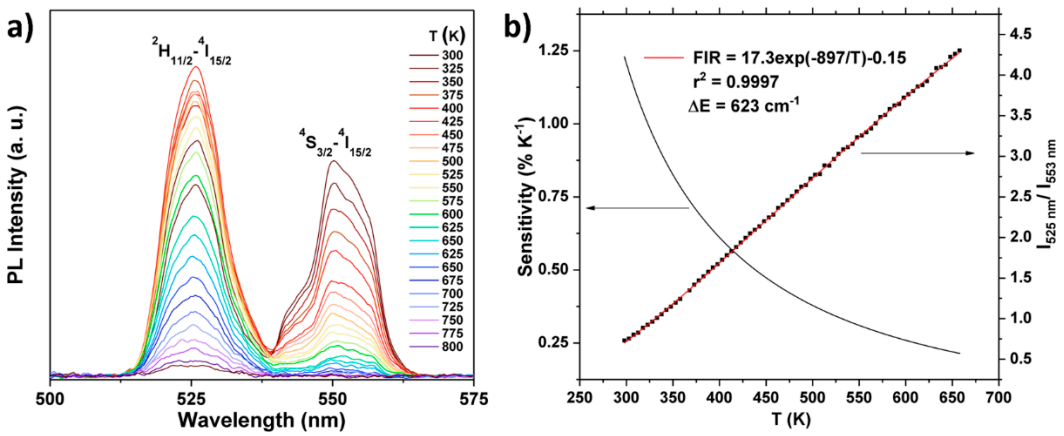

Figure 10. (a) Emission spectra of YVO_4:1%Er^{3+} in the temperature range 300–800 K. (b) The temperature dependence of the FIR between the emission peaks at 525 nm ($^2H_{11/2}$–$^4I_{15/2}$) and 553 nm ($^4S_{3/2}$–$^4I_{15/2}$). The red line

 doi:10.20944/preprints202603.1041.v1

shows the best fit for the experimental data (black squares) to the equation: FIR. The black solid line shows the corresponding relative temperature sensitivity. Reproduced with permission from Ref. [93] under Creative Commons Attribution 4.0 International License.

5. Sensing Applications: Recent Advances

Sensing applications of vanadates have been previously illustrated and discussed. This section provides a brief overview of significant developments in the field since 2023.

Vanadate materials – including binary oxides such as V_2O_5, ternary compounds like $BiVO_4$, and various transition-metal vanadates (e.g., Zn–, Fe–, Pr–vanadates) – are semiconductors characterized by tunable electronic structure, high redox activity, and versatile surface chemistry. These properties render them highly effective for a range of chemical sensing applications, particularly in gas detection and electrochemical identification of complex analytes.

Vanadium pentoxide, for instance, exhibits a wide bandgap (2.3 eV), a robust chemical and thermal stability, a rich surface chemistry and a characteristic metal–insulator transition at 257 °C. As detailed in a comprehensive review of V_2O_5 gas sensors [96], these devices operate primarily through three mechanisms: gas adsorption, polaron hopping and direct chemical interaction. These mechanisms facilitate diverse applications in environmental monitoring, food safety, medical diagnostics and pharmaceutics. Recent literature [97] emphasizes that the high surface-to-volume ratio and inherent reactivity of V_2O_5 allow for the selective detection of biomolecules and other analytes at sub-ppm concentrations. Furthermore, its distinctive lamellar structure is highly conducive to doping, enabling direct modification of its structural and optical characteristics. Incorporating multiple rare-earth (RE) elements can induce cooperative effects that enhance optical performance and expand functionality [98]. For instance, annealed films constituted by CeO_2:V_2O_5 nano-particles have recently demonstrated high sensitivity in thin film strain-gauge applications due to their optimized electrical and morphological characteristics [99].

Bismuth vanadate is an n-type semiconductor nanomaterial with a narrow bandgap (2.4 eV), making it highly active under visible light. While being a promising catalyst for rapid removal of pollutants from wastewater [100], $BiVO_4$ has emerged as a potent biosensing platform, due to its unique electrochemical properties, high dispersibility, high photocatalytic efficiency, low toxicity, and biocompatibility. Recent developments highlight its efficacy in detecting various disease biomarkers with high sensitivity and specificity [101]. Additionally, morphology-tailored $BiVO_4$ nanostructures have shown improved gas-sensing performance for environmental monitoring (e.g., NO_x, H_2S) by maximizing surface active sites and oxygen vacancies [102].

The zircon-type tetragonal structure of certain vanadates acts as a stable host lattice for dopant ions. Materials such as YVO_4, $GdVO_4$, and $LuVO_4$ have emerged as premier materials for optical sensing due to their unique combination of structural stability and exceptional spectroscopic properties. Unlike other hosts, the vanadate group (VO_4^{3-}) is "self-activated", absorbing ultraviolet (UV) light and efficiently transferring energy to lanthanide dopants, thus significantly enhancing luminescence. These materials maintain structural integrity at high temperatures (melting points near 1800°C) and are resistant to chemical degradation, making them ideal for sensing in harsh environments. Recent advances in the synthesis and applications of RE-doped phosphors, including vanadates have been discussed in literature [103–105].

Figure 11 shows schematically the luminescence processes in RE-doped AVO_4 and $ANbO_4$ phosphors (where A= Y, Gd, or La for niobate, and A= Y or Gd for vanadate) [103]. The very intense emission upon UV and NIR excitation may be exploited for producing high-security anti-counterfeiting inks. These 'invisible' inks remain covert under ambient light but emit intense fluorescence under UV or near-infrared (NIR) excitation. An advance in documents' security is possible by integrating optical authentication provided by the ink's fluorescence and biometric recognition through fingerprint patterns. Efficient detection of latent fingerprints, with low background interferences, was made possible by the RE ions' capability of multi-color emission [106–109].

 doi:10.20944/preprints202603.1041.v1

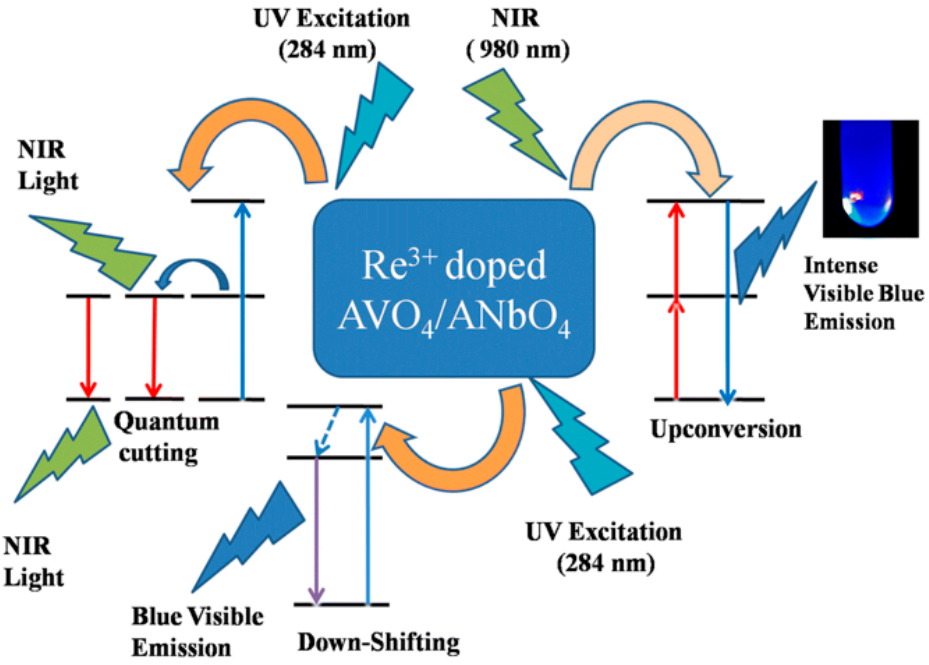

Figure 11. Schematic representation of the spectral conversion processes which may occur in RE-doped vanadate and niobate materials upon UV or NIR excitation. A= Y or Gd for vanadate, and A= Y, Gd, or La for niobate. Image reproduced from [103] under CC BY license.

For example, Ye et al. [107] developed various $GdVO_4:RE^{3+}$ through a dual sintering process at 1100°C. CIE color coordinates diagram for $GdVO_4$-doped with trivalent Bi, Dy, Eu, Bi/Dy, Bi/Tm and Bi/Eu ions is shown in Figure 12. The $GdVO4:Bi^{3+}/Eu^{3+}$ formulation proved particularly resistant to background interference, enabling the resolution of latent fingerprint details on various surfaces and under hard humidity and temperature conditions. Because these nanoparticles are significantly (1000–10,000 times) smaller than the width of a fingerprint ridge, they enable exceptional spatial resolution and superior adhesion. Recent studies on a set of nanocrystalline red light-emitting $Ca_8ZnGd_{1-x}Eu_x(VO_4)_7$ (x = 0.10–0.50 mol), synthesized via a non-hazardous and cost-effective solution-based calcination (SBC) route have shown promising results [109]. XRD analysis confirmed that Eu^{3+} ions were diffused into the trigonal host matrix without causing structural deformation. The size of non-uniform agglomerated particles was evaluated around 61 nm. The chromaticity coordinates of the optimal sample ($Ca_8ZnGd_{0.80}Eu_{0.20}(VO_4)_7$) and its high color purity of 97.7% indicate that this material stands at the forefront of both fluorescence-based forensic sensing and advanced optoelectronic devices.

As a general trend, RE-doped vanadates have gained significant interest for luminescence thermometry and chemical biosensing. In most cases, the luminescence intensity ratio (LIR) technique is used. This ratiometric approach calculates absolute temperature by comparing the intensity of two distinct emission peaks (e.g., from Eu^{3+} or Nd^{3+}), effectively neutralizing fluctuations in excitation laser power. Beyond LIR, thermal sensing can also be performed by monitoring temperature-dependent shifts in spectral line position and line bandwidth. Significant research over the last decade has demonstrated the efficacy of various nanostructures, including $YVO_4:Nd^{3+}$ [79] and $La_3Sc_2Ga_3O_{12}:Cr^{3+}/Nd^{3+}$, nanophosphors [110], YVO_4: Ho^{3+}/Yb^{3+} nanocrystals [111], $GdVO_4:Er^{3+}/Yb^{3+}$ nanocrystalline powders [112], and (Y, Yb, Tm, Er)VO_4 systems [113].

In a recent study, a RE-doped solid solution of yttrium phosphate-vanadate ($YV_{1-x}P_xO_4:Eu^{3+}$, Er^{3+}) was proposed as a high-performance luminescent thermometer [114]. This material leverages the strong, broad charge transfer absorption of the vanadate group to sensitize RE^{3+} ions. It facilitates multi-mode sensing by utilizing: the LIR of Er^{3+} $^2H_{11/2}/^4S_{3/2}$ emission, the dual-center LIR of integrated Er^{3+} and Eu^{3+} emission intensities, and the emission lifetime of Eu^{3+}. This system enables very accurate

 doi:10.20944/preprints202603.1041.v1

temperature sensing across a wide temperature range, from room temperature to 873 K; inside that range, the P/V ratio (x) is adjustable to optimize performance for specific thermal windows.

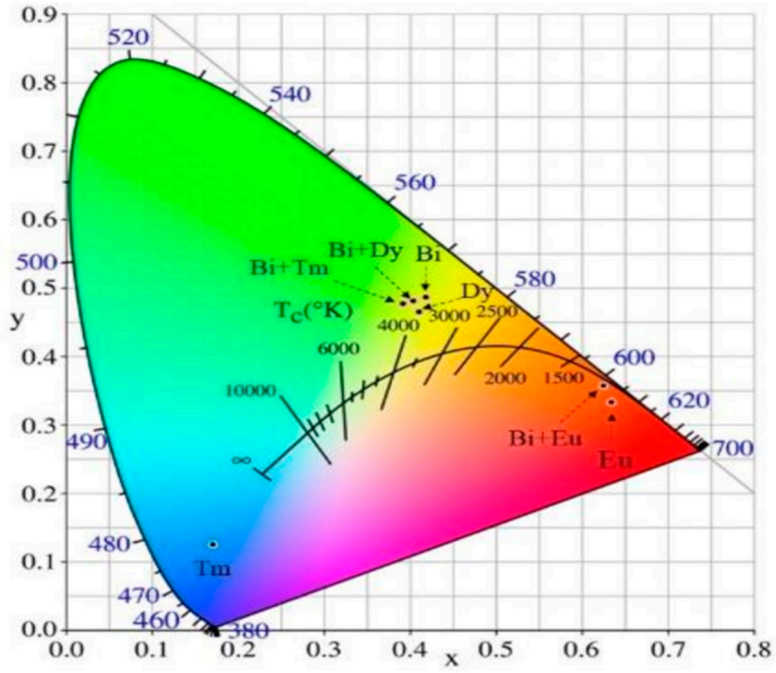

Figure 12. CIE color coordinates of gadolinium vanadate doped with heavy metal (Bi) and different rare earths (Dy, Eu, Tm) or a combination of them (Bi+Dy, Bi+Eu, Bi+Tm). Reproduced from [107] under CC BY license.

While the LIR method is easy to be implemented and is robust against experimental or sample-related conditions, such as fluctuations in excitation intensity, sample geometry, or concentration of luminescent probes, concerns have been raised about its absolute precision. Vieira Perrella et al. [115] addressed this issue by synthesizing UV-excitable Eu^{3+}-doped yttrium vanadate and phosphovanadate ($Y(V,P)O_4$) particles. Their work clarified how the intrinsic spectral overlap between $^3T_{1,2} \rightarrow {}^1A_1$ VO_4^{3-} transitions and Eu^{3+} transitions $^5D_0 \rightarrow {}^7F_J$ impacts sensor reliability. Without a proper baseline correction, the broad band background overlap can result in a ten-fold increase in temperature uncertainty and a ~60% underestimation of relative thermal sensitivity.

Vanadate compounds are increasingly used for the detection and remediation of persistent pollutants in aquatic ecosystems, often related to pharmaceutical residuals eliminated by humans and animals through their bodily waste. This issue has become crucial due to the disproportionate usage of antimicrobial agents in humans, animals and in feed supplements. The photocatalytic activity of pure $Ca_2V_2O_7$ has shown remarkable results under visible light irradiation [116]. Within 180 min, this material achieved 79.5% removal of safranin O (a red cationic dye used in histology and Gram-bacteria staining) and 80.6% removal of tetracycline hydrochloride (a yellow, crystalline, broad-spectrum antibiotic) [116]. In addition, $Ca_2V_2O_7$ nanomaterial was effective for photocatalytic hydrogen generation.

RE-vanadates are emerging as superior electrochemical probes for the precise quantification of various biological and pharmaceutical compounds. Sriram et al. [117] performed a comparative study of hydrothermally synthesized TVO_4 (T = Ho, Y, Dy) for the simultaneous detection of two representative drugs, namely, nitrofurazone (an antiseptic drug towards urinary tract infection) and roxarsone (an organo-arsenic drug, used in poultry as feed additive). The three RE-vanadates were found to respond differently, and results demonstrated that $DyVO_4$-based electrodes exhibited superior sensitivity, achieving exceptionally low detection limits (0.002 μM for nitrofurazone and 0.0009 μM for roxarsone). Similarly, orthovanadates (RE-VO_4, where RE = Pr, Gd, and Sm) were evaluated for the detection of two antibiotics, i.e., furazolidone (FD) and metronidazole (MD), nitro-functional synthetic drugs that have been in use for over 30 years [118]. Using differential pulse

 doi:10.20944/preprints202603.1041.v1

voltammetry, the different vanadates were compared as electrode modifiers and $SmVO_4$-modified glassy carbon electrode emerged as the most effective, characterized by the lowest charge transfer resistance (R_{ct} = 56.82 Ω) and the largest electrochemical surface area (A = 0.11 cm^2). This sensor not only provided the lowest limits of detection (0.0009 μM for FD and 0.0036 μM for MD individually, and 0.0015 μM and 0.0049 μM for simultaneous detection) but also showed excellent anti-interference, repeatability, and reproducibility. A recent comparative analysis of RE-doped molybdate, tungstate, and vanadate nanomaterials for the detection and photocatalytic degradation of nitrofurantoin (NFT), a persistent and toxic antibiotic contaminant, highlighted the versatility of these materials [119]. A series of $NaDy(MoO_4)_2$:Tb^{3+}, $NaDy(WO_4)_2$:Tb^{3+}, and $Na_3Dy(VO_4)_2$:Tb^{3+} nanomaterials were synthesized via a hydrothermal method and systematically characterized. While the tungstate variant excelled in the photocatalytic degradation of NFT under UV light (96% degradation in 60 min), the vanadate variant exhibited the highest sensitivity for NFT detection, with a detection limit of 0.38 ppm.

6. Conclusions

This paper has provided a comprehensive overview of advances in synthesis strategies, luminescent properties and sensing applications of the Ln-doped rare-earth vanadate materials: A detailed discussion is given regarding the preparation such as solid state reactions, coprecipitation, hydrothermal/solvothermal, sol-gel, microwave-assisted methods. The main attention has been focused on their structures properties, especially optical, downconversion and upconversion luminescence and their sensing application perspectives of these materials.

The Ln^{3+}-activated nanomaterials have emerged as versatile platforms for biodetection, fluorescence *in vitro* and *in vivo* bioimaging and therapeutic applications including anti-aging, antibacterial, anticancer and antioxidant effects. Their performance is driven by advances in host materials such as $GdVO_4$, YVO_4, and $LuVO_4$, alongside innovations in design, size, shape, co-doping and surface modification. As a result, Ln^{3+}-activated nanomaterials are gaining increasing importance in biomedical research, with rapid progress expected through continued developments in materials synthesis, surface engineering and assay technologies.

Vanadates activated by Ln^{3+} ions and co-doped with (Yb^{3+} or Nd^{3+}), so-called upconverting materials, have broader sensing application potential, beyond biomedicine and advanced sensing technologies. They have been applied in luminescence imaging, cell labeling, magnetic resonance imaging, photodynamic therapy, chemotherapy, single-photon emission computed tomography, X-ray computed tomography, optical biosensing, biomarker identification, immunoassays, drug delivery, luminescence thermometry, solar energy conversion, fingerprint detection, photocatalysis, and related fields. In biomedical contexts, upconverting nanomaterials offer distinct advantages, including deeper tissue penetration, minimal autofluorescence background, reduced scattering and absorption, excellent photostability, and negligible photoblinking.

Looking ahead, the main research on Ln-doped vanadate materials should be focus on the integrating multimodal biomedical functions, while ensuring biocompatibility for clinical applications and shifting of excitation wavelengths from 980 nm to safer biological windows (808 nm) to reduce tissue heating.

Author Contributions: Conceptualization, D.M. and M.F.; methodology, D.M.; software, G.C.R. and M.F.; validation, D.M., G.C.R., and M.F.; resources, D.M. and M.F.; writing—original draft preparation, D.M. and M.F.; writing—review and editing, D.M., G.C.R., and M.F.; funding acquisition, D.M. and M.F. All authors have read and agreed to the published version of the manuscript.

Funding: This research was supported by the Ministry of Science, Technological Development and Innovation of the Republic of Serbia (grant number 451-03-33/2026-03/200017).

 doi:10.20944/preprints202603.1041.v1

Data Availability Statement: This review article does not contain any original data. All data referenced in this article are publicly available from the sources cited in the references. No new datasets were generated or analyzed in this work.

Conflicts of Interest: The authors declare no conflicts of interest.

References

1. Ma, X.-F.; Li, H.-Y.; Ren, W.; Gao, D.; Chen, F.; Diao, J.; Xie, B.; Huang, G.; Wang, J.; Pan, F. A critical review of vanadium-based electrode materials for rechargeable magnesium batteries. *J. Mater. Sci. Tech.* **2023**, *153*, 56-74, https://doi.org/10.1016/j.jmst.2022.12.052
2. Silva-Ramírez, G.A.; Garrido-Hernández, A.; Carrera-Jota, M.L.; García-Hernández, M.; Hernández-Fuentes, C.F.; Morales-Ramírez, A.J. Differences in structural and luminescent properties of $GdVO_4:Sm^{3+}$, Bi^{3+} powder and sol-gel derived films with varying Sm^{3+} contents and annealing temperatures. *Ceram. Int.* **2025**, *51*, 8913-8929, https://doi.org/10.1016/j.ceramint.2024.12.322
3. Sisó-Moliné, R.; Cascales, C.; Méndez, M.; Fuentes-Rodriguez, L.; de Aquino, A.; Pujol, M.C.; Zaldo, C.; Carvajal, J.J. Preparation and characterization of $GdVO_4$:Tb,Eu nanoparticles/carbon dots composites via hydrothermal deposition and physical mixing for luminescent nanothermometry. *Adv. Mater. Interfaces* **2025**, *12*, e00410, https://doi.org/10.1002/admi.202500410
4. Hrabovsky, J.; Kucera, M.; Palousova, L.; Zazvorka, J.; Kubat, J.; Bi, L.; Veis, M. Rapid and precise large area mapping of rare-earth doping homogeneity in luminescent materials. *Commun. Mater*. **2024**, *5*, 251. https://doi.org/10.1038/s43246-024-00679-x
5. Soharab, M.; Bhatt, R.; Benerji, N.S.; Bhaumik, I. Comparison of optical properties and self Q-switched lasing in Cr-Nd co-doped $GdVO_4$ and YVO_4 single crystals. *Physica B: Condens. Matter*. **2025**, *707*, 417171, https://doi.org/10.1016/j.physb.2025.417171
6. Dahiya, B.; Nain, S. Structural and dielectric properties of rare earth-doped $GdVO_4$/ZnO composites for opto-electronic applications. *Ceram. Int.* **2025**, *51*, 21448-21460, https://doi.org/10.1016/j.ceramint.2025.02.304
7. Li, M.; Li, J.-G. Extensive tailoring of $REPO_4$ and $REVO_4$ crystallites *via* solution processing and luminescence. *CrystEngComm*. **2022**, *24*, 4841-4852, https://doi.org/10.1039/D2CE00535B
8. Yan, H.; Shao, E.; Qi, X.; Du, Y.; Wang, C. Low-temperature bonding of Nd: YVO_4 crystals with superior interfaces for high-power solid-state lasers. *Appl. Surf. Sci.* **2025**, *703*, 163426, https://doi.org/10.1016/j.apsusc.2025.163426
9. Kruczek, M.; Talik, E.; Sakowska, H.; Ujma, Z.; Skrzypek D. XPS investigations of YVO_4:Tm,Yb single crystal. *J. Crystal Growth* **2005**, *275*, e1715-e1720, https://doi.org/10.1016/j.jcrysgro.2004.11.250
10. Dai, W.; Liu, T.; Ding, Y.; Zhao, Y.; Zhang, Y. High-efficiency Nd:$LuVO_4$ laser at 1343 nm recycling-pumped by a laser diode at 916 nm. *Front. Phys.* **2024**, *12*, 1388372, https://doi.org/10.3389/fphy.2024.1388372
11. Jovanović, D.J.; Chiappini, A.; Zur, L.; Gavrilović, T.V.; Tran, T.N.L.; Chiasera, A.; Lukowiak, A.; Smits, K.; Dramićanin, M.D.; Ferrari, M. Synthesis, structure and spectroscopic properties of luminescent $GdVO_4:Dy^{3+}$ and $DyVO_4$ particles. *Opt. Mater.* **2018**, *76*, 308-316, https://doi.org/10.1016/j.optmat.2017.12.046
12. Antić, Ž.; Dramićanin, M.D.; Prashanthi, K.; Jovanović, D.; Kuzman, S.; Thundat, T. Pulsed laser deposited dysprosium-doped gadolinium–vanadate thin films for noncontact, self-referencing luminescence thermometry. *Adv. Mater.* **2016**, *28*, 7745-7752, https://doi.org/10.1002/adma.201601176
13. Gavrilović, T.V.; Jovanović, D.J.; Smits, K.; Dramićanin, M.D. Multicolor upconversion luminescence of $GdVO_4:Ln^{3+}/Yb^{3+}$ (Ln^{3+} = Ho^{3+}, Er^{3+}, Tm^{3+}, $Ho^{3+}/Er^{3+}/Tm^{3+}$) nanorods. *Dyes Pigm.* **2016**, *126*, 1-7, https://doi.org/10.1016/j.dyepig.2015.11.005
14. del Rosal, B.; Perez-Delgado, A.; Misiak, M.; Bednarkiewicz, A.; Vanetsev, A.S.; Orlovskii, Y.; Jovanović, D.J.; Dramićanin, M.D.; Rocha, U.; Kumar, K.U.; Jacinto, C.; Navarro, E.; Rodriguez, E.M.; Pedroni, M.; Speghini, A.; Hirata, G. A.; Martin, I.R.; Jaque, D.; Neodymium-doped nanoparticles for infrared fluorescence bioimaging: The role of the host. *J. Appl. Phys.* **2015**, *118*, 143104 (11pp), https://doi.org/10.1063/1.4932669

 doi:10.20944/preprints202603.1041.v1

15. Pan, X.; Hu, M.; Wu, L.; Wei, E.; Zhu, Q.; Lv, L.; Xv, X.; Dong, X.; Liu, H.; Liu, Y. Biomedical applications of gadolinium-containing biomaterials: Not only MRI contrast agent. *Adv Sci. (Weinh)* **2025**, *12*, 2501722, https://doi.org/10.1002/advs.202501722
16. Mahata, M.K.; Kumar, K.; Rai, V.K. Er^{3+}–Yb^{3+} doped vanadate nanocrystals: A highly sensitive thermographic phosphor and its optical nanoheater behaviour. *Sens. Actuators B Chem.* **2015**, *209* 775–780, https://doi.org/10.1016/j.snb.2014.12.039
17. Kabbani, M.A.; Tiwary, C.S.; Autreto, P.A.S.; Brunetto, G.; Som, A.; Krishnadas, K.R.; Ozden, S.; Hackenberg, K.P.; Gong, Y.; Galvao, D.S.; Vajtai, R.; Kabbani, A.T.; Pradeep, T.; Ajayan, P.M. Ambient solid-state mechano-chemical reactions between functionalized carbon nanotubes. *Nature Commun.* **2015**, *6*, 7291, https://doi.org/10.1038/ncomms8291
18. Huang, Z.; Zhang, L.; Pan, W. Synthesis, lattice dynamics, and mechanical properties of a high-pressure scheelite phase of RVO_4. *Inorg. Chem*. **2012**, *51*, 11235-11237, https://doi.org/10.1021/ic3017672
19. Gavrilović, T.V.; Jovanović, D.J.; Trandafilović, L.V.; Dramićanin, M.D. Effects of Ho^{3+} and Yb^{3+} doping concentrations and Li^{+} co-doping on the luminescence of $GdVO_4$ powders. *Opt. Mater.* **2015**, *45*, 76–81, https://doi.org/10.1016/j.optmat.2015.03.013
20. Huignard, A.; Gacoin, T.; Boilot, J.-P. Synthesis and luminescence properties of colloidal YVO_4:Eu phosphors. *Chem. Mater.* **2000**, *12*, 1090–1094, https://doi.org/10.1021/cm990722t
21. Tang, S.; Huang, M.; Wang, J.; Yu, F.; Shang, G.; Wu, J. Hydrothermal synthesis and luminescence properties of $GdVO_4$:Ln^{3+} (Ln = Eu, Sm, Dy) phosphors. *J. Alloys Compd*. **2012**, *513*, 474-480, https://doi.org/10.1016/j.jallcom.2011.10.093
22. Xu, Z.; Feng, B.; Gao, Y.; Zhao, Q.; Sun, D.; Gao, X.; Li, K.; Ding, F.; Sun, Y. Uniform and well-dispersed $GdVO_4$ hierarchical architectures: hydrothermal synthesis, morphology evolution, and luminescence properties. *CrystEngComm.* **2012**, *14*, 145530-5538, https://doi.org/10.1039/C2CE25521A
23. Li, X.-B.; Geng, Y.-C.; Wang, A.-Q.; Xi B.-Y.; Zhang, J.-Q.; Dang, W.-Q.; Ling, W.-J.; Dong, Z. Preparation of zircon type GdVO and study of its gas sensitivity properties. *Ceram. Int.* **2025**, *51*, 59138-59148, https://doi.org/10.1016/j.ceramint.2025.10.132
24. Silva-Ramírez, G.A.; Garrido-Hernández, A.; Carrera-Jota, M.L.; García-Hernández, M.; Hernández-Fuentes, C.F.; Morales-Ramírez, A.J. Differences in structural and luminescent properties of $GdVO_4$:Sm^{3+}, Bi^{3+} powder and sol-gel derived films with varying Sm^{3+} contents and annealing temperatures. *Ceram. Int.* **2025**, *51*, 8913-8929, https://doi.org/10.1016/j.ceramint.2024.12.322
25. Roopana, S.M.; Thangapandi Chellapandia, Shebeer, R.M.; Akhil, E.; Alappat, J.D.; Nair, N.R.; Madhusoodanan, M.; Chitra, D. Advances and prospects in the development of $GdVO_4$-based photocatalysts for water pollutants removal activity: A review. *Nano Mater. Sci.* **2025**, *7*, 180–197, https://doi.org/10.1016/j.nanoms.2024.04.001
26. Chumha, N.; Kittiwachana, S.; Thongtem, T.; Thongtem, S.; Kaowphon, S. Synthesis and characterization of $GdVO_4$ nanostructures by a tartaric acid-assisted sol–gel method. *Ceram. Int.* **2014**, 16337-16342, https://doi.org/10.1016/j.ceramint.2014.07.072
27. Dhakal, D.R.; Kshetri, Y.K.; Chaudhary, B.; Choi, J.-h.; Murali, G.; Kim, T.H. Enhancement of upconversion luminescence in Yb^{3+}/Er^{3+}-doped $BiVO_4$ hrough calcination. *Mater. Today Commun.* **2023**, 37, 107258, https://doi.org/10.1016/j.mtcomm.2023.107258
28. Godinho, M.; Ribeiro, C.; Longo, E; Leite, E.R. Influence of microwave heating on the growth of gadolinium-doped cerium oxide nanorods. *Cryst. Growth Des.* **2008**, 8, 384–386, https://doi.org/10.1021/cg700872b
29. Sung-Myung Ryu, Chunghee Nam, Shape-controlled microwave hydrothermal synthesis of antiferromagnetic $GdVO_4$ nanowires for magnetocaloric materials. *Curr. Appl. Phys.* **2020**, *20*, 715-719, https://doi.org/10.1016/j.cap.2020.03.005
30. Thakur, H.; Singh, R.K.; Gathania, A.K. Synthesis and optical properties of $GdVO_4$: Eu^{3+} phosphor. *Mater. Res. Express* **2021**, *8*, 026201, https://doi.org/10.1088/2053-1591/abe221
31. Unoki, H. The secondary effect of the cooperative Jahn-Teller distortion in rare earth vanadate. *J. Magn. Magn. Mater*. **1983**, *31-34*, 1063-1064, https://doi.org/10.1016/0304-8853(83)90798-9

 doi:10.20944/preprints202603.1041.v1

32. Lotfi, S.; Ouardi, M.E.; Ahsaine, H.A.; Madigou, V.; BaQais, A.; Assani, A.; Saadi, M.; Arab, M. Low-temperature synthesis, characterization and photocatalytic properties of lanthanum vanadate $LaVO_4$. *Heliyon* **2023**, *9*, e17255, https://doi.org/10.1016/j.heliyon.2023.e17255
33. Guo, H.; Lu, Q.; Xie, J.; Wu, D.; Chen, Z. Energy transfer mechanism and optical properties of Eu^{3+}, Dy^{3+} co-doped $LaVO_4$ phosphors. *Spectrochim. Acta A Mol. Biomol. Spectrosc.* **2025**, *339*, 126292, https://doi.org/10.1016/j.saa.2025.126292
34. Vasylechko, L.; Tupys, A.; Hreb, V.; Tsiumra, V.; Lutsiuk, I.; Zhydachevskyy, Y. New mixed $Y_{0.5}R_{0.5}VO_4$ and RVO_4:Bi materials: Synthesis, crystal structure and some luminescence properties. *Inorganics* **2018**, *6*(3), 94, https://doi.org/10.3390/inorganics6030094
35. Chen, B. Luminescent materials with advanced properties and applications. *Inorganics* **2024**, *12(12)*, 306; https://doi.org/10.3390/inorganics12120306
36. Li, J.; Tian, X.; Bao, W.; Zhao, J.; Jiang, Z. Recent advances in the development and applications of lanthanide-based luminescent materials: a comprehensive review. *Discov Appl Sci*. **2025**, *7*, 1310 https://doi.org/10.1007/s42452-025-07862-w
37. Eker, F.; Duman, H.; Akdaşçi, E.; Bolat, E.; Sarıtaş,S.; Karav, S.; Witkowska, A.M. A comprehensive review of nanoparticles: from classification to application and toxicity. *Molecules* **2024**, *29(15)*, 3482; https://doi.org/10.3390/molecules29153482
38. Ragupathi, C.; Narayanan, S.; Tamizhdurai, P.; Sukantha, T.A.; Ramalingam, G.; Pachamuthu, M.P.; Mangesh, V.L.; Kumar, N.S.; Al-Fatesh, A.S.; Kasim, S.O. Correlation between the particle size, structural and photoluminescence spectra of nano $NiCr_2O_4$ and La doped $NiCr_2O_4$ materials. *Heliyon* **2023**, *9(11)*, e21981. https://doi.org/10.1016/j.heliyon.2023.e21981
39. Warutkar, G.; Ugemuge, N.; Ansari, E.; Pusdekar, A.; Dhale, S.; Tumram, P.; Patle, S.; Moharil, S.V. Synthesis and spectroscopic analysis in $GdVO_4$:RE^{3+} (RE=Sm, Eu) by solid state metathesis for optical applications. *J. Mol. Struct.* **2025**, *1332*, 141591. https://doi.org/10.1016/j.molstruc.2025.141591
40. Kaowphong, S.; Chumha, N.; Nimmanpipug, P.; Kittiwachana, S. Nanosized $GdVO_4$ powders synthesized by sol–gel method using different carboxylic acids. *Rare Met.* **2018**, *37*, 561–567 https://doi.org/10.1007/s12598-015-0681-4
41. Mazierski, P.; Sowik, J.; Miodyńska, M.; Trykowski, G.; Mikołajczyk, A.; Klimczuk, T.; Lisowski,W.; Nadolna, J.; Zaleska-Medynska, A. Shape-controllable synthesis of $GdVO_4$ photocatalysts and their tunable properties in photocatalytic hydrogen generation. *Dalton Trans.* **2019**, *48*, 1662-1671. https://doi.org/10.1039/C8DT04225J
42. Xu, H.Y.; Wang, H.; Meng, Y. Q.; Yan, H. Rapid synthesis of size-controllable YVO_4 nanoparticles by microwave irradiation. Solid State Commun. **2004**, *130*, 465-468. https://doi.org/10.1016/j.ssc.2004.02.045
43. Tomina, E.V.; Sladkopevtsev, B.V.; Novikova, L.A.; Boykov N.I.; Maltsev, S.A. Microwave and ultrasonic radiation-activated synthesis and luminescent properties of nanopowder YVO_4:Bi^{3+},Eu^{3+}. *Russ Chem Bull* **2023**, 72, 1113–1121 https://doi.org/10.1007/s11172-023-3879-x
44. Zhu, Z.; Han, S.; Cao, Y.; Jiang, J. Synthesis of a novel photocatalyst MVO_4/g-C_3N_4 (M = La, Gd) with better photocatalytic activity for tetracycline hydrochloride degradation under visible-light irradiation. *Crystals* **2021**, *11*(7), 756. **https://doi.org/10.3390/cryst11070756**
45. Li, G.; Jiang, S.; Liu, A.; Ye, L.; Ke, J.; Liu, C.; Chen, L.; Liu Y.; Hong, M. Proof of crystal-field-perturbation-enhanced luminescence of lanthanide-doped nanocrystals through interstitial H^+ doping. *Nat. Commun.* **2023**, *14*, 5870. https://doi.org/10.1038/s41467-023-41411-6
46. Kimani, M.; Colin, M.; McMillen, D.; Kolis, J.W. Synthetic and spectroscopic studies of vanadate glaserites II: Photoluminescence studies of Ln:$K_3Y(VO_4)_2$ (Ln=Eu, Er, Sm, Ho, or Tm). *J. Solid State Chem.* **2015**, *226*, 320-325. https://doi.org/10.1016/j.jssc.2015.01.012
47. Chen, Z.; Zhu, H.; Qian, J.; Li, Z.; Hu, X.; Guo, Y.; Fu, Y.; Zhu, H.; Nai, W.; Yang, Z.; Li, D.; Zhou L. Rare earth ion doped luminescent materials: a review of up/downconversion luminescent mechanism, synthesis, and anti-counterfeiting application. *Photonics* **2023**, *10*, 1014. https://doi.org/10.3390/photonics10091014
48. Jovanović, D.J.; Gavrilović, T.V.; Dolić, S.D.; Marinović-Cincović, M.; Smits, K.; Dramićanin, M.D. Up-conversion luminescence of $GdVO^4$:Nd^{3+}/Er^{3+} and $GdVO_4$:Nd^{3+}/Ho^{3+} phosphors under 808 nm excitation. *Opt. Mater.* **2018**, *82*, 1-6. https://doi.org/10.1016/j.optmat.2018.05.033

 doi:10.20944/preprints202603.1041.v1

49. Chen, Z.; Zhu, H.; Qian, J.; Li, Z.; Hu, X.; Guo, Y.; Fu, Y.; Zhu, H.; Nai, W.; Yang, Z.; Li, D.; Zhou L. Rare earth ion doped luminescent materials: a review of up/downconversion luminescent mechanism, synthesis, and anti-counterfeiting application. *Photonics* **2023**, *10*, 1014. https://doi.org/10.3390/photonics10091014
50. Han, S.; Tao, Y.; Du, Y.; Yan, S.; Chen, Y.; Chen, D. Luminescence behavior of $GdVO_4$:Tb nanocrystals in silica glass-ceramics. *Crystals* **2020**, *10(5)*, 396; https://doi.org/10.3390/cryst10050396
51. Jovanović, D.J.; Antić, Ž.; Krsmanović, R.M.; Mitrić, M.; Đorđević, V.; Bártová, B.; Dramićanin, M.D. Annealing effects on the microstructure and photoluminescence of Eu^{3+}-doped $GdVO_4$ powders. *Opt. Mater.* **2013**, *35*, 1797–1804. https://doi.org/10.1016/j.optmat.2013.03.012
52. González-Penguelly, B.; Pérez-Sánchez, G.G.; Medina-Velázquez, D.Y.; Martínez-Falcón, P.; Morales-Ramírez, A.J. Luminescence properties and energy transfer of Eu^{3+}, Bi^{3+} co-doped $LuVO_4$ films modified with Pluronic F-127 obtained by sol–gel. *Materials* **2023**, *16(1)*, 146. https://doi.org/10.3390/ma16010146
53. Chi, F.; Ji, Z.; Liu, Q.; Jiang, B.; Wang, B.; Cheng, J.; Li, B.; Liu, S.; Wei, X. Investigation of multicolor emitting $Cs_3GdGe_3O_9$:Bi^{3+},Eu^{3+} phosphors *via* energy transfer for WLEDs. *Dalton Trans.* **2023**, *52*, 635-643. https://doi.org/10.1039/D2DT03349F
54. Tu, D.; Zheng, W.; Huang, P.; Chen, X. Europium-activated luminescent nanoprobes: From fundamentals to bioapplications. *Coord. Chem. Rev.* **2019**, *378*, 104–120. https://doi.org/10.1016/j.ccr.2017.10.027
55. Tkachenko, A.; Yefimova, S.; Tryfonyuk, L.; Thomas, S. Nanostructured vanadates as Janus-faced redox-active nanomaterials: Biological effects and molecular mechanisms. *Biol. Trace Elem. Res*. **2026**, In Press. https://doi.org/10.1007/s12011-025-04947-w
56. Kot, Y.; Klochkov, V.; Prokopiuk, V.; Sedyh, O.; Tryfonyuk, L.; Grygorova, G.; Karpenko, N.M Tomchuk, O.; Kot, K.; Onishchenko, A.; Yefimova, S.; Tkachenko, A. $GdVO_4$:Eu^{3+} and $LaVO_4$:Eu^{3+} nanoparticles exacerbate oxidative stress in L929 cells: potential implications for cancer therapy. *Int. J. Mol. Sci.* **2024,** 25(21), 11687. https://doi.org/10.3390/ijms252111687
57. Hu, H.; Li, D.; Liu, S.; Wang, M.; Moats, R.; Conti, P.S.; Li, Z. Integrin $\boldsymbol{\alpha_2\beta_1}$ targeted $GdVO_4$:Eu ultrathin nanosheet for multimodal PET/MR imaging. *Biomaterials* **2014**, *35*, 8649-8658. http://dx.doi.org/10.1016/j.biomaterials.2014.06.059
58. Toro-González, M.; Dame, A.N.; Mirzadeh, S.; Rojas, J.V. Gadolinium vanadate nanocrystals as carriers of α-emitters (^{225}Ac, ^{227}Th) and contrast agents. *J. Appl. Phys.* **2019**, *125*, 214901. https://doi.org/10.1063/1.5096880
59. Toro-González, M.; Copping, R.; Mirzadeh, S.; Rojas, J.V. Multifunctional $GdVO_4$:Eu core–shell nanoparticles containing ^{225}Ac for targeted alpha therapy and molecular imaging. *J. Mater. Chem. B* **2018**, ***6***, 7985-7997. https://doi.org/10.1039/C8TB02173B
60. Hyunsub Kim, Heejin Jeong, Song-Ho Byeon, Selective filter effect induced by Cu^{2+} adsorption on the fluorescence of a $GdVO_4$:Eu nanoprobe. *ACS Appl. Mater. Interfaces* **2016**, *8*, 15497–15505. https://doi.org/10.1021/acsami.6b03960
61. Liang, Y.; Noh, H.M.; Park, S.H.; Choi, B.C.; Jeong, J.H. Colloidal $GdVO_4$:Eu^{3+}@SiO_2 nanocrystals for highly selective and sensitive detection of Cu^{2+} ions. https://doi.org/10.1039/C8TB02173B
62. Periša, J.; Antić, Ž.; Ma, C.-G.; Papan, J.; Jovanović, D.; Dramićanin, M.D. Pesticide-induced photoluminescence quenching of ultra-small Eu^{3+}-activated phosphate and vanadate nanoparticles *J. Mater. Sci. Technol.* **2020**, *38*, 197–204. https://doi.org/10.1016/j.jmst.2019.09.004
63. Muhr, V.; Buchner, M.; Hirsch, T.; Jovanović, D.J.; Dolić, S.D.; Dramićanin, M.D.; Wolfbeis, O.S. Europium-doped $GdVO_4$ nanocrystals as a luminescent probe for hydrogen peroxide and for enzymatic sensing of glucose. *Sens. Actuator B Chem.* **2017**, *241*, 349-356. https://doi.org/10.1016/j.snb.2016.10.090
64. Maksimchuk, P.O.; Hubenko, K.O.; Knupfer, M.; Seminko, V.V.; Klochkov, V.K.; Sorokin, O.V.; Demchenko, L.D.; Yefimova S.L. Microscopic mechanisms of luminescence quenching in Eu^{3+}-doped $GdVO_4$ nanoparticles under hydrogen peroxide decomposition. *J. Mol. Liq.* **2024**, *400*, 124510. https://doi.org/10.1016/j.molliq.2024.124510
65. Proiou, E.; Pinakidou, F.; Paloura, E.C.; Pétri, N.; Gacoin, T.; Laplace-Builhé, C.; Schuck, G.; Alexandrou, A.; Katsikini, M. Spatial distribution and stability of $Gd_{0.6}Eu_{0.4}VO_4$ nanoparticles injected in mouse ear pinnae. *TrAC Trends Anal. Chem.* **2025**, *182*, 118049. https://doi.org/10.1016/j.trac.2024.118049

 doi:10.20944/preprints202603.1041.v1

66. Li, N.; Yang, B.; Guo, L.; Li, T. $Na_3Gd(VO_4)_2$:Yb^{3+}/(Er^{3+}, Tm^{3+}, Ho^{3+}) and $Na_3Gd(VO_4)_2$: Yb^{3+}/Er^{3+}/(La^{3+}, Lu^{3+}, Y^{3+}): Upconversion luminescence and temperature sensitivity under single- and multi-wavelength excitation. *Bull. Mater. Sci.* **2023**, *46*, 222. https://doi.org/10.1007/s12034-023-03058-3
67. Min, B.H.; Jung, K.Y. Enhanced upconversion luminescence of $GdVO_4$:Er^{3+}/Yb^{3+} prepared by spray pyrolysis using organic additives. *RSC Adv.* **2019**, *9*, 20002-20008. https://doi.org/10.1039/C9RA03941D
68. Prasad, M.; Rai, V.K. Thermally stable upconverting $Na_3Zr_2(SiO_4)_2PO_4$:Er^{3+}/Yb^{3+} phosphors for displays and optical thermometry. *J. Alloys Compd.* **2022**, *911*, 164968. https://doi.org/10.1016/j.jallcom.2022.164968
69. Gavrilović, T.V.; Jovanović, D.J.; Lojpur, V.; Dramićanin, M.D. Multifunctional Eu^{3+} and Er^{3+}/Yb^{3+}-doped $GdVO_4$ nanoparticles synthesized by reverse micelle method. *Sci. Rep.* **2014**, *4*, 4209. https://doi.org/10.1038/srep04209
70. Stopikowska, N.; Runowski, M.; Woźny, P.; Lis, S.; Du, P. Generation of pure green up-conversion luminescence in Er^{3+} doped and Yb^{3+}-Er^{3+} co-doped YVO_4 nanomaterials under 785 and 975 nm excitation. *Nanomaterials* **2022**, *12(5)*, 799. https://doi.org/10.3390/nano12050799
71. Zharkov, D.K.; Leontyev, A.V.; Shmelev, A.G.; Nurtdinova, L.A.; Chuklanov, A.P.; Nurgazizov, N.I.; Nikiforov, V. G. Upconversion luminescence response of a single YVO_4:Yb, Er particle. *Micromachines* **2023**, *14*(5), 1075. https://doi.org/10.3390/mi14051075
72. Maurya, A.; Yadav, R.S.; Yadav, R.V.; Rai, S.B.; Bahadur, A. Enhanced green upconversion photoluminescence from Ho^{3+}/Yb^{3+} co-doped $CaZrO_3$ phosphor via Mg^{2+} doping, *RSC Adv.* **2016**, *6*, 113469-113477. https://doi.org/10.1039/C6RA23835A
73. Yadav, M.R.S.; Bahadur, A.; Rai, S.B. Near-infrared light excited highly pure green upconversion photoluminescence and intrinsic optical bistability sensing in a Ho^{3+}/Yb^{3+} co-doped $ZnGa_2O_4$ phosphor through Li^+ doping. *J. Phys. Chem. C* **2020**, *124*, 10117–10128. https://doi.org/10.1021/acs.jpcc.0c01554
74. Gavrilović, T.V.; Nikolić, M.G.; Jovanović, D.J.; Dramićanin, M.D. Up-conversion luminescence of Tm^{3+} sensitized by Yb^{3+} ions in $GdVO_4$. *Phys. Scr. T* **2013**, *157*, 014055. https://doi.org/10.1088/0031-8949/2013/T157/014055
75. Savchuk, O.; Marti, J.J.C.; Cascales, C.; Haro-Gonzalez, P.; Sanz-Rodríguez, F.; Aguilo, M.; Diaz, F. Bifunctional Tm^{3+},Yb^{3+}:$GdVO_4$@SiO_2 core-shell nanoparticles in HeLa cells: Upconversion luminescence nanothermometry in the first biological window and biolabelling in the visible. *Nanomaterials* **2020**, *10(5)*, 993. https://doi.org/10.3390/nano10050993
76. Liu, B.; Li, C.; Yang, P.; Hou, Z.; Lin, J. 808-nm-light-excited lanthanide-doped nanoparticles: rational design, luminescence control and theranostic applications. *Adv. Mater.* **2017**, *29*, 1605434. https://doi.org/10.1002/adma.201605434
77. Zhai, T.; Zhang, Y.; Guan, D.; Yang, L.; Zhang, W.; Zhang, Y.; Liu, Q. Investigation of upconversion luminescence attenuation in aqueous solutions under 980 nm and 808 nm irradiation. *J. Anal. Test.* **2023**, *7*, 377–383. https://doi.org/10.1007/s41664-023-00281-z
78. Xu, C.; Wu, R.; Xiao, Z.; Xu, L. Thermal analysis of phonons assisted bright yellow upconversion emission and one photon near-infrared upconversion emission in Nd^{3+} doped $GdVO_4$ single crystals. *Ceram. Int.* **2024**, *50*, 42619-42624. https://doi.org/10.1016/j.ceramint.2024.08.105
79. Kolesnikov, I.E.; Kalinichev, A.A.; Kurochkin, M.A.; Golyeva, E.V.; Kolesnikov, E.Y.; Kurochkin, A.V.; Lähderanta, E.; Mikhailov, M.D. YVO_4:Nd^{3+} nanophosphors as NIR-to-NIR thermal sensors in wide temperature range. *Sci. Rep.* **2017**, 7, 18002. https://doi.org/10.1038/s41598-017-18295-w
80. Rosal, B. del.; Pérez-Delgado, A.; Carrasco, E.; Jovanović, D.J.; Dramićanin, M.D.; Dražić, de la Fuente, G.Á.J.; Sanz-Rodriguez, F.; Jaque, D. Neodymium-based stoichiometric ultrasmall nanoparticles for multifunctional deep-tissue photothermal therapy. *Adv. Optical Mater.* **2016**, *4*, 782–789. https://doi.org/10.1002/adom.201500726
81. Hong, G.; Antaris, A.; Dai, H. Near-infrared fluorophores for biomedical imaging. *Nat. Biomed. Eng.* **2017**, *1*, 0010. https://doi.org/10.1038/s41551-016-0010
82. Ansari, A.A.; Thakur, V.K.; Chen, G. Functionalized upconversion nanoparticles: New strategy towards FRET-based luminescence bio-sensing. *Coord. Chem. Rev.* **2021**, *436*, 213821. https://doi.org/10.1016/j.ccr.2021.213821

 doi:10.20944/preprints202603.1041.v1

83. Zajdel, K.; Janowska, J.; Frontczak-Baniewicz, M.; Sypecka, J.; Sikora, B. Upconverting nanoparticles as a new bio-imaging strategy—Investigating intracellular trafficking of endogenous processes in neural tissue**.** *Int. J. Mol. Sci.* **2023**, *24(2)*, 1122. https://doi.org/10.3390/ijms24021122
84. Wang, W.; Shang, S.; Wang, Y.; Xu, B. Utilization of nanomaterials in MRI contrast agents and their role in therapy guided by imaging. *Front. Bioeng. Biotechnol.* **2024**, *12*, 1484577. https://doi.org/10.3389/fbioe.2024.1484577
85. Zheng, W.T.; Chen, H.L.; Hou, X.T.; Abakirova, A.; Han, M.-Y.; Feng, Y.-Q.; Huang, W.-T.; Mo, X.-C.; Zhu, H.-C.; Huang, S.-K.; Lv, H.-D.; Yang, T.; Huang, S.; Shi, Z.-M. Research trends and hotspots of upconversion nanoparticles for drug delivery and biomedical targeting in photodynamic therapy. *Discover. Nano* **2025**, *20*, 235. https://doi.org/10.1186/s11671-025-04402-8
86. Thao, C.T.B.; Huy, B.T.; Sharipov, M.; Kim, J-I.; Dao, V-D.; Moon, J-Y.; Lee, Y-I. Yb^{3+}, Er^{3+}, Eu^{3+}-codoped YVO_4 material for bioimaging with dual mode excitation. *Mater. Sci. Engin. C* **2017**, *75*, 990-997. https://doi.org/10.1016/j.msec.2017.02.169
87. Lv, Z.; Jin, L.; Cao, Y.; Zhang, H.; Xue, D.; Yin, N.; Zhang, T.; Wang, Y.; Liu, J.; Liu, X.; Zhang, H. A nanotheranostic agent based on Nd^{3+}-doped YVO_4 with blood-brain-barrier permeability for NIR-II fluorescence imaging/magnetic resonance imaging and boosted sonodynamic therapy of orthotopic glioma. *Light Sci. Appl.* **2022**, *29*, 116. https://doi.org/10.1038/s41377-022-00794-9
88. Carbonati, T.; Ciontia, C.; Cosaert, E.; Nimmegeers, B.; Meronia, D.; Poelman, D. NIR emitting $GdVO_4$:Nd nanoparticles for bioimaging: The role of the synthetic pathway. *J. Alloys Compd.* **2021**, *862*, 158413. https://doi.org/10.1016/j.jallcom.2020.158413
89. Yin, W.; Zhou, L.; Gu, Z.; Tian, G.; Jin, S.; Yan, L.; Liu, X.; Xing, G.; Ren, W.; Liu, F.; Pan, Z.; Zhao, Y. Lanthanide-doped $GdVO_4$ upconversion nanophosphors with tunable emissions and their applications for biomedical imaging. *J. Mater. Chem.* **2012**, *22*, 6974-6981. https://doi.org/10.1039/C2JM16152D
90. Pavitra, E.; Lee, H.; Hwang, S.K.; Park, J.Y.; Han, Y-K.; Raju, G.S.R.; Huh, Y.S. Evolution of highly biocompatible and thermally stable YVO_4:Er^{3+}/Yb^{3+} upconversion mesoporous hollow nanospheriods as drug carriers for therapeutic applications. *Nanomaterials* **2022**, *12*, 2520. https://doi.org/10.3390/nano12152520
91. Jaque, D.; Vetrone, F. Luminescence nanothermometry. *Nanoscale* **2012**,*.4*, 4301–4326. https://doi.org/10.1039/C2NR30764B
92. Mahata, M.K.; Koppe, T.; Kumar, K.; Hofsäss, H.; Vetter, U. Demonstration of temperature dependent energy migration in dual-mode YVO_4:Ho^{3+}/Yb^{3+} nanocrystals for low temperature thermometry. *Sci Rep.* **2016**, *6*, 36342. https://doi.org/10.1038/srep36342
93. Getz, M.N.; Nilsen, O.; Hansen, P.-A. Sensors for optical thermometry based on luminescence from layered YVO_4:Ln^{3+} (Ln = Nd, Sm, Eu, Dy, Ho, Er, Tm, Yb) thin films made by atomic layer deposition. *Sci Rep.* **2019**, *9*, 10247. https://doi.org/10.1038/s41598-019-46694-8
94. Debasu, M.L.; Ananias, D.; Pastoriza-Santos, I.; Liz-Marzán, L.M.; Rocha, J.; Carlos, L.D. All-in-one optical heater-thermometer nanoplatform operative from 300 to 2000 K based on Er^{3+} emission and blackbody radiation. *Adv. Mater.* **2013**, *.25*, 4868-4874. https://doi.org/10.1002/adma.201300892
95. Fischer, L.H.; Harms, G.S.; Wolfbeis, O.S. Upconverting nanoparticles for nanoscale thermometry. *Angew. Chem. Int. Ed. Engl.* **2011**, *50*, 4546–4551. https://doi.org/10.1002/anie.201006835
96. Alrammouz, R.; Lazerges, M.; Pironon, J.; Bin Taher, I.; Randi, A.; Halfaya, Y.; Gautier, S. V_2O_5 gas sensors: A review. *Sens. Actuators A: Phys.* **2021**, *332*, 113179. https://doi.org/10.1016/j.sna.2021.113179
97. Chackrabarti, S.; Zargar, R.A. Review: vanadium pentoxide thin films-advanced doping strategies and interface engineering for next-generation applications. *J Mater Sci* **2026**, 61, 4894–4938. https://doi.org/10.1007/s10853-026-12152-w
98. Abdelrazek MM; Abd-Elrazek ME; El Refaay DE; El-Desoky M.M. Enhanced optical properties of V_2O_5 thin films through rare earth co-doping. *Physica B* **2025**, *699*, 416881. https://doi.org/10.1016/j.physb.2024.416881
99. Kishan Chand, T.R.; Kalpana, H.M.; Satish, T.N. Effect of thickness and annealing on electrical characteristics of cerium oxide-doped vanadium oxide (CeO_2:V_2O_5) thin film for sensor application. *J Mater Sci: Mater Electron* **2024**, *35*, 616. https://doi.org/10.1007/s10854-024-12388-9

 doi:10.20944/preprints202603.1041.v1

100. Marinković, D.; Righini, G.C.; Ferrari, M. Synthesis, optical, and photocatalytic properties of the $BiVO_4$ semiconductor nanoparticles with tetragonal zircon-type structure. *Photonics* **2025**, *12*, 438. https://doi.org/10.3390/photonics12050438
101. Poovethamkandiyil, A.S.; Palliyalil, K.K.; Sujith, K.; Paravannoor, A.; Ganguly, P.; Vijayan, B. K. Emerging bismuth vanadate-based biosensor platforms for diagnostic, imaging, therapeutic and antibacterial applications. *J. Mater. Chem. B* **2025**, *13*, 13928–13953. https://doi.org/10.1039/D5TB01332A
102. Sagadevan, S.; T. Soga, T. Morphology-dependent gas sensing properties of bismuth vanadate nano-materials: A promising approach for environmental monitoring. *Inorg. Chem. Commun.* **2024**, *160*, 111980. https://doi.org/10.1016/j.inoche.2023.111980
103. Dwivedi, A.; Roy, A.; Rai, S. B. Photoluminescence behavior of rare earth doped self-activated phosphors (ie niobate and vanadate) and their applications. *RSC Adv.* **2023**, *13*, 16260-16271. https://doi.org/10.1039/D3RA00629H
104. Kiran, R.; Kamath, N.; Sayyed, M. I.; Almuqrin, A. H.; Kamath, S. D. A review of recent developments in rare earth-doped nanophosphors for emerging technological applications. *RSC Adv.* **2025**, *15*, 20040-20060. https://doi.org/10.1039/D5RA03126E
105. Ugemuge, N. S.; Bhagat, R. M.; Warutkar, G.; Dhale, S.; Pimpalkar, A.; Mistry, A.; Selokar, A.W.; Bishnoi, S.; Golhar, A.; Dhoble, S. J. Recent advances in vanadate phosphor materials: synthesis and optoelectronic applications: A comprehensive review. *J. Electron. Mater.* **2025**, *54*, 8185-8217. https://doi.org/10.1007/s11664-025-12206-w
106. Liu, J.; Huang, Z.; Zhang, Z.; Zhu, D.; Yue, C.; Li, K. Near-ultraviolet activated dual-functional $Na_3Sc_2(VO_4)_3$ phosphors with Eu^{3+}/Sm^{3+} dopant systems for multimodal anti-counterfeiting and ratiometric optical thermal sensing. *J. Alloys Compd.* **2025**, *1031*, 181107. https://doi.org/10.1016/j.jallcom.2025.181107
107. Ye, Y.; Liang, J.; Zhang, W.; Xie, W.; Feng, Z.; Hu, Z.; Xiong, G.; Liu, Z. Synthesis and luminescence properties of Bi^{3+} and Re^{3+} (Re= Eu, Dy, Tm) co-doped $GdVO_4$ phosphors for latent fingerprint detection. *J. Phys.: Conf. Ser. 2024 2920*, 012002 http://doi.org/10.1088/1742-6596/2920/1/012002
108. Devi, P.; Dalal, H.; Sehrawat, N.; Solanki, D.; Malik, R. K. Phase identification and photophysical characteristics of vanadate-based nanophosphors for lighting and latent fingerprinting applications. *Inorg. Chem. Commun.* **2024**, *168*, 112885. https://doi.org/10.1016/j.inoche.2024.112885
109. Sehrawat, N.; Devi, P.; Solanki, D.; Kumari, N.; Punia, R.; Malik, R. K.; Garg, S. Crystal structure and photophysical analysis of red emitting Eu^{3+} doped vanadate based nanomaterials for innovative optoelectronic devices and latent fingerprinting applications. *Inorg. Chem. Commun.* **2026**, *186*, 116318. https://doi.org/10.1016/j.inoche.2026.116318
110. Xie, X.; Ge, W.; Tian, Y.; Zhang, Q.; Yang, M.; Wu, C.; He, P.; Yin, H. $La_3Sc_2Ga_3O_{12}:Cr^{3+}$, Nd^{3+} near-infrared phosphor for nondestructive detection and luminescence thermometry. *Ceram. Int.* ***2024****, 50(22),* 46098-46106. https://doi.org/10.1016/j.ceramint.2024.08.454
111. Mahata, M. K.; Koppe, T.; Kumar, K.; Hofsäss, H.; Rai, V. K.; Schneider, J. Demonstration of temperature dependent energy migration in dual-mode $YVO_4:Ho^{3+}/Yb^{3+}$ nanocrystals for low temperature thermometry. *Sci. Rep.* **2016**, *6*, 36342. https://doi.org/10.1038/srep36342
112. Paz-Buclatin, F.; Rivera-Lopez, F.; Gonzalez, O.; Martin, I.R.; Martin, L.L.; Jovanovic, D.J. $GdVO_4:Er^{3+}/Yb^{3+}$ nanocrystalline powder as fluorescence temperature sensor. Application to monitor the temperature of an electrical component. *Sens. Actuators A: Phys*. **2019,** *299*, 111628. https://doi.org/10.1016/j.sna.2019.111628
113. Perrella, R. V.; de Sousa Filho, P. C. *High-sensitivity dual UV/NIR-excited luminescence thermometry by rare earth vanadate nanoparticles.* ***Dalton Trans.*** **2020**, *49*, 911–921. https://doi.org/10.1039/C9DT04308J.
114. Ma, Y.; Zhou, X.; Wu, J.; Dong, Z.; Cui, L.; Wang, Y.; Meijerink, A. Luminescence thermometry via multiparameter sensing in $YV_{1-x}P_xO_4:Eu^{3+}$, Er^{3+}. *J. Am. Chem. Soc.* **2025**, *147*, 12925– 12936. https://doi.org/10.1021/jacs.5c02306
115. Vieira Perrella, R.; Derroso, G.; de Sousa Filho, P.C. Improper background treatment underestimates thermometric performance of rare earth vanadate and phosphovanadate nanocrystals. *ACS Omega* **2024**, *9*, 34974–34980. https://doi.org/10.1021/acsomega.4c04835

 doi:10.20944/preprints202603.1041.v1

116. Tripathy, A.; Kumari, K.H.; Pati, S.; Veldurthi, N.K. Visible-light driven multifunctional $Ca_2V_2O_7$ photocatalyst for sustainable hydrogen generation and degradation of organic pollutants. *Photochem Photobiol Sci* **2026**. https://doi.org/10.1007/s43630-026-00864-6
117. Sriram, B.; Baby, J. N.; Hsu, Y.-F.; Wang, S.-F.; George, M. Scheelite-type rare earth vanadates TVO_4 (T = Ho, Y, Dy) electrocatalysts: Investigation and comparison of T site variations towards bifunctional electrochemical sensing application. *Chem. Engin. J.* **2023**, *451*, 138694. https://doi.org/10.1016/j.cej.2022.138694
118. Bharathi, P.; Wang, S.F. Rare earth orthovanadate (REM-VO_4; REM = Pr, Gd, and Sm)-based sensors for selective and simultaneous detection of furazolidone and metronidazole. *Nanoscale* **2025**, *17*, 5907–5924. https://doi.org/10.1039/D4NR04594G
119. Bhagat, N.; Niharika; Devi, S.; Singhaal, R.; Sen, C.; Sheik H.N. Hydrothermal synthesis and dual functional performance of $NaDy(MoO_4)_2$:Tb^{3+}, $NaDy(WO_4)_2$:Tb^{3+}, and $Na_3Dy(VO_4)_2$:Tb^{3+} nanomaterials for nitrofurantoin sensing and photocatalytic degradation. *J. Mater. Sci: Mater. Electron.* **2025**, *36*, 1736. https://doi.org/10.1007/s10854-025-15803-x